

Sparse Functional Identification of Complex Cells from Spike Times and the Decoding of Visual Stimuli

Aurel A. Lazar Nikul H. Ukani

Yiyin Zhou*

Department of Electrical Engineering

Columbia University

New York, NY 10027

aurel, nikul, yiyin@ee.columbia.edu

December 4, 2017

Abstract

We investigate the sparse functional identification of complex cells and the decoding of spatio-temporal visual stimuli encoded by an ensemble of complex cells. The reconstruction algorithm is formulated as a rank minimization problem that significantly reduces the number of sampling measurements (spikes) required for decoding. We also establish the duality between sparse decoding and functional identification, and provide algorithms for identification of low-rank dendritic stimulus processors. The duality enables us to efficiently evaluate our functional identification algorithms by reconstructing novel stimuli in the input space. Finally, we demonstrate that our identification algorithms substantially outperform the generalized quadratic model, the non-linear input model and the widely used spike-triggered covariance algorithm.

Keywords: encoding of visual stimuli, complex cells, quadratic receptive fields, dendritic stimulus processors, sparse neural decoding, sparse functional identification, duality between decoding and functional identification

*The authors' names are listed in alphabetical order.

Contents

1	Introduction	4
2	Neural Circuits with Complex Cells: Encoding, Decoding and Functional Identification	6
2.1	Modeling Temporal Stimuli	6
2.2	Encoding of Temporal Stimuli by a Population of Complex Cells	7
2.3	Decoding of Temporal Stimuli Encoded by a Population of Complex Cells . .	9
2.4	Functional Identification of DSPs of Complex Cells	10
3	Low-Rank Decoding and Functional Identification	11
3.1	Low-Rank Decoding of Stimuli	12
3.1.1	Exploiting the Structure of Complex Cell Encoding	12
3.1.2	Reconstruction Algorithms	13
3.1.3	Example - Decoding of Temporal Stimuli Encoded with a Population of Complex Cells	16
3.1.4	Example - IAF Spike Generators with Random Thresholds	17
3.1.5	Example - Hodgkin-Huxley Neurons as Biophysical Spike Generators	18
3.1.6	Example - Hodgkin-Huxley Neurons with Stochastic Ion Channels . .	19
3.2	Low-Rank Functional Identification of Complex Cells	19
3.2.1	Duality Between Low-Rank Functional Identification and Decoding .	19
3.2.2	Functional Identification Algorithms	21
3.2.3	Example - Identification of Complex Cell DSPs from Spike Times .	23
3.3	Evaluation of Functional Identification of a Neural Circuit of Complex Cells by Decoding	24
4	Low-Rank Decoding and Functional Identification of Complex Cells with Spatio-Temporal Stimuli	25
4.1	Low-Rank Decoding of Spatio-Temporal Visual Stimuli	26
4.1.1	Example - Decoding of 2D Spatio-Temporal Stimuli	26
4.1.2	Example - Decoding of 3D Spatio-Temporal Stimuli	27
4.2	Low-Rank Functional Identification of Spatio-Temporal Complex Cells . .	29
4.2.1	Example - Low-Rank Functional Identification of Complex Cell DSP from Spike Times in Response to Spatio-Temporal Stimuli	29
4.2.2	Example - Evaluation of Functional Identification of Neural Circuit of Complex Cells Using Decoding	31
4.2.3	Comparison with STC, GQM and NIM	31
5	Conclusions	32
A	Proof of Lemma 2	38
B	Modeling of Spatio-Temporal Stimuli	38
C	Encoding of Spatiotemporal Stimuli with a Population of Complex Cells	39

1 Introduction

It is widely accepted that the early mammalian visual system employs a series of neural circuits to extract elementary visual features, such as edges and motion [1, 2]. Feature extraction capabilities of simple and complex cells arising in the primary visual cortex (V1) have been extensively investigated. Layer IV simple cells receive direct input from the Lateral Geniculate Nucleus [3]. Each simple cell consists of a linear receptive field cascaded with a highly-nonlinear spike generator. Complex cells in layer II/III of V1 sum the output of a pool of simple cells having similar orientation selectivity and spatial extent [4] and are thereby selective to oriented edges/lines over a spatially restricted region of the visual field [1]. While simple cells respond maximally to a particular phase of the edge, complex cells are largely phase invariant [5, 6]. Therefore, the receptive fields of complex cells cannot be simply mapped into excitatory and inhibitory regions [1]. Receptive fields of simple cells are often modeled as spatio-temporal linear filters with a spatial impulse response that resemble Gabor functions [7], whereas the receptive fields of complex cells are often modeled as a sum of squared linear filters [8]. For simplicity, a quadrature pair of space-time Gabor filters has been employed in an energy model of complex cells [9, 10, 11]. Neural circuits comprising complex cells constitute a highly nonlinear circuit as illustrated in Figure 1.

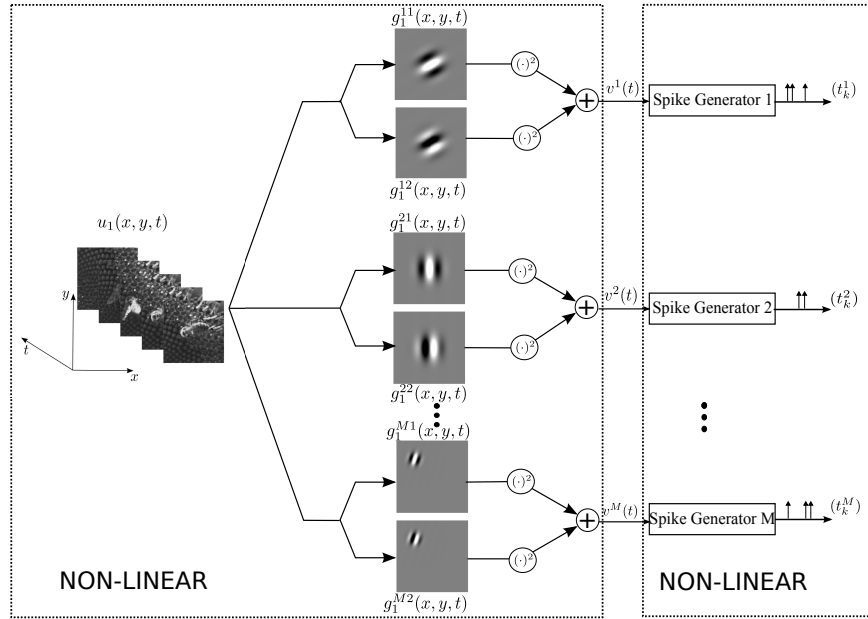


Figure 1: A neural circuit consisting of a population of complex cells.

Feedforward projections from V1 to other cortical areas mainly originate from layer II/III [12], suggesting that complex cells play a critical role in relaying visual information processed in V1 to higher brain areas. While tuning properties of individual complex cells have been characterized [13, 14], the information about visual stimuli that an ensemble of complex cells can provide, and how efficiently they can represent such information has yet to be elucidated.

Under the modeling framework of Time Encoding Machines (TEMs) [15, 16], it has been shown that decoding of stimuli and functional identification of linear receptive fields of simple

cells are dual to each other [17]. This led to mathematically rigorous identification algorithms for identifying linear receptive fields of simple cells [17]. By modeling the nonlinear processing in complex cells as Volterra Dendritic Stimulus Processors (DSPs) [18, 19], the representation of stimuli encoded by spike times generated by neural circuits with complex cells was also exhaustively analyzed. Functional identification of a complex cell DSP was possible again thanks to the demonstrated duality between decoding and functional identification. While these theoretical methods exhibit deep structural properties, they have been shown to be tractable only for decoding and functional identification problems of small dimensions. In their current form they are not tractable due to the “curse of dimensionality” [20].

The non-linear transformations taking place in the DSP of complex cells lead to loss of phase information. Previous work has empirically found that static images recovered from the magnitude response of Gabor wavelets are perceptually recognizable, albeit they exhibit significant errors in their pixel intensity values [43]. Here, we formulate the reconstruction of stimuli encoded with complex cells as a phase retrieval problem [21] and, in search of tractable algorithms, utilize recent developments in optimization theory of low-rank matrices [22, 23, 21]. By applying such methods, we develop algorithms that are highly effective in decoding visual stimuli encoded by complex cells. As will be detailed in the next sections, the complex cells, as defined in this paper, have DSP kernels that are low-rank and include the ones shown in Figure 1 as a particular case.

After demonstrating that the decoding of visual stimuli becomes tractable, we describe sparse algorithms that functionally identify the DSPs of complex cells using the spike times they generate. The sparse identification algorithms are based on the key observation that functional identification can be viewed as the dual problem of decoding stimuli that are encoded by an ensemble of complex cells. While the generalization of the duality results from simple cells to complex cells was already given in [18], we show in this paper that these results remain valid under the assumption of sparsity, that is, for the case of low-rank DSP kernels. This significantly reduces the time of stimulus presentation that is needed in the identification process. The sparse duality result also enables us to evaluate the identified circuits in the input space. We achieve the latter by computing the mean square error or signal-to-noise ratio (SNR) of novel stimuli decoded using the identified circuits [17]. The sparse decoding and functional identification algorithms presented here apply to circuits build around a wide range of neurons models including Integrate-and-Fire neurons with random thresholds and biophysically realistic conductance-based models with intrinsic noise.

This paper is organized as follows. In Section 2, we first introduce the modeling of encoding of temporal stimuli with complex cells. We provide a detailed review of decoding of stimuli and the functional identification of complex cells, and point out the current algorithmic limitations. In Section 3, we provide sparse decoding algorithms that achieve high accuracy and are algorithmically tractable. We then explicate the dual relationship between sparse functional identification and decoding and provide examples for the identification of low-rank, temporal DSP kernels of complex cells. In Section 4, we extend sparse decoding methodology to spatio-temporal stimuli and functional identification of spatio-temporal complex cells. Using novel stimuli, we provide evaluation examples of the identification algorithms in the input space as well as comparisons to other state-of-the-art methods. Finally, we conclude in Section 5 and suggest how the approach advanced in this paper can be applied beyond

complex cells.

2 Neural Circuits with Complex Cells: Encoding, Decoding and Functional Identification

In this section, we model the encoding of temporal stimuli by a neural circuit consisting of neurons akin to complex cells. We start by modeling the space of temporal stimuli in Section 2.1. In Section 2.2, the model of encoding is formally described. In Section 2.3, we proceed to present a reconstruction algorithm for decoding temporal stimuli encoded by the neural circuit. A method for functional identification of neurons constituting the neural circuit is provided in Section 2.4. The reconstruction algorithm and the functional identification algorithm discussed in this section are based on [18].

2.1 Modeling Temporal Stimuli

We model the temporal varying stimuli $u_1 = u_1(t)$, $t \in \mathbb{D}$, to be real-valued elements of the space of trigonometric polynomials [15]. The choice of the space of the trigonometric polynomials has, as we will see, substantial computational advantages.

Definition 1. *The space of trigonometric polynomials \mathcal{H}_1 is the Hilbert space of complex-valued functions*

$$u_1(t) = \sum_{l_t=-L_t}^{L_t} c_{l_t} e_{l_t}(t), \quad (1)$$

over the domain $\mathbb{D} = [0, S_t]$, where

$$e_{l_t}(t) = \frac{1}{\sqrt{S_t}} \exp\left(\frac{j l_t \Omega_t}{L_t} t\right)$$

and $c_{l_t}, l_t = -L_t, \dots, L_t$, are the coefficients of u_1 in \mathcal{H}_1 . Here Ω_t denotes the bandwidth, and L_t the order of the space. Stimuli $u_1 \in \mathcal{H}_1$ are extended to be periodic over \mathbb{R} with period $S_t = 2\pi L_t / \Omega_t$.

We denote the dimension of \mathcal{H}_1 by $\dim(\mathcal{H}_1)$ and $\dim(\mathcal{H}_1) = 2L_t + 1$.

Definition 2. *The tensor product space $\mathcal{H}_2 = \mathcal{H}_1 \otimes \mathcal{H}_1$ is a Hilbert space of complex-valued functions*

$$u_2(t_1; t_2) = \sum_{l_{t_1}=-L_t}^{L_t} \sum_{l_{t_2}=-L_t}^{L_t} d_{l_{t_1} l_{t_2}} e_{l_{t_1}}(t_1) \cdot e_{l_{t_2}}(t_2) \quad (2)$$

over the domain $\mathbb{D}^2 = [0, S_t] \times [0, S_t]$, where $d_{l_{t_1} l_{t_2}}, l_{t_1} l_{t_2} \in \mathbb{D}^2$, are the coefficients of u_2 in \mathcal{H}_2 .

Note that $\dim(\mathcal{H}_2) = \dim(\mathcal{H}_1)^2$.

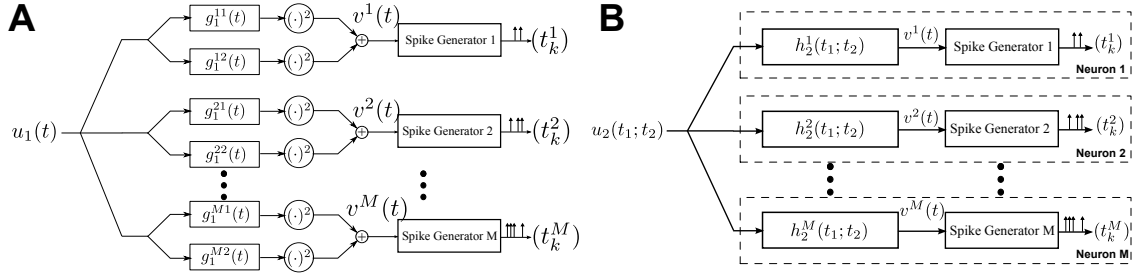


Figure 2: The encoding of temporal stimuli by a neural circuit modeling an ensemble of complex cells. (A) The i^{th} neuron in the model processes the input $u_1(t)$ by two parallel linear filters with impulse responses $g_1^{i1}(t)$ and $g_1^{i2}(t)$, respectively, followed by squaring. The outputs are summed and then fed into a spike generator. (B) An equivalent representation of the encoding circuit in which the DSPs are represented as second-order Volterra kernels.

2.2 Encoding of Temporal Stimuli by a Population of Complex Cells

We consider a neural circuit consisting of M neurons as shown in Figure 2A. For the i^{th} neuron, input stimulus $u_1(t)$ ($u_1 \in \mathcal{H}_1$) is first processed by two linear filters with impulse responses $g_1^{i1}(t)$ and $g_1^{i2}(t)$, the outputs of which are individually squared and then summed together. These processing elements are integral part of the DSP of neuron i [18, 19]. The output of the DSP i , denoted by $v^i(t)$, is then fed into the Biological Spike Generator (BSG) of neuron i . The BSG i encodes the output of DSP i into the spike train $(t_k^i)_{k \in \mathbb{I}^i}$. Here \mathbb{I}^i is the spike train index set of neuron i . We notice the similarity between the overall structure of neural circuits in Figure 2A and Figure 1. In what follows, we refer to the neurons in the neural circuit in Figure 2A as complex cells.

The output of the DSP of the i^{th} neuron in Figure 2A amounts to

$$v^i(t) = \left[\int_{\mathbb{D}} g_1^{i1}(t-s_1) u_1(s_1) ds_1 \right]^2 + \left[\int_{\mathbb{D}} g_1^{i2}(t-s_2) u_1(s_2) ds_2 \right]^2, \quad (3)$$

for all $i = 1, 2, \dots, M$.

With

$$h_2^i(t_1; t_2) = g_1^{i1}(t_1) g_1^{i1}(t_2) + g_1^{i2}(t_1) g_1^{i2}(t_2), \quad (4)$$

(3) can be rewritten as

$$v^i(t) = \int_{\mathbb{D}^2} h_2^i(t-s_1; t-s_2) u_1(s_1) u_1(s_2) ds_1 ds_2, \quad (5)$$

where $h_2^i(t_1; t_2)$ is interpreted as a second-order Volterra kernel [24]. We assume that $h_2^i(t_1; t_2)$ is real, bounded-input bounded-output (BIBO) stable, causal and of finite memory. The I/O of the neural circuit shown in Figure 2A can be equivalently outlined as in Figure 2B, in which each neuron processes the input $u_1(t)$ nonlinearly by a second order kernel $h_2^i(t_1; t_2)$ followed by a BSG.

Remark 1. Note that the BSG models the spike generation mechanism of the axon hillock of a biological neuron, whereas the DSP is an equivalent model of processing of the stimuli by a sophisticated neural network that proceeds the spike generation. Therefore, stimulus processing and the spike generation mechanism are naturally separated in the neuron model considered here.

For simplicity, we first formulate the spike generation mechanism of the encoder as an ideal Integrate-and-Fire (IAF) (point) neuron (see, e.g., [17]). The integration constant, bias and threshold of the IAF neuron $i = 1, 2, \dots, M$, is denoted by κ^i , b^i and δ^i , respectively. The mapping of the input amplitude waveform $v^i(t)$ into the time sequence $(t_k^i)_{k \in \mathbb{Z}}$ is called the t-transform [15]. For the i -th neuron, the t-transform is given by [15, 16]:

$$\int_{t_k^i}^{t_{k+1}^i} v^i(t) dt = \kappa^i \delta^i - b^i (t_{k+1}^i - t_k^i). \quad (6)$$

Lemma 1. The encoding of the temporal stimulus $u_1 \in \mathcal{H}_1$ into the spike train sequence $(t_k^i), k \in \mathbb{I}^i, i = 1, 2, \dots, M$, by a neural circuit with complex cells is given in functional form by

$$\mathcal{T}_k^i u_2 = q_k^i, k \in \mathbb{I}^i, i = 1, \dots, M, \quad (7)$$

where M is the total number of neurons, $n_i + 1$ is the number of spikes generated by neuron i and $\mathcal{T}_k^i : \mathcal{H}_2 \rightarrow \mathbb{R}$, are bounded linear functionals defined by

$$\mathcal{T}_k^i u_2 = \int_{t_k^i}^{t_{k+1}^i} \int_{\mathbb{D}^2} h_2^i(t - s_1; t - s_2) u_2(s_1; s_2) ds_1 ds_2 dt, \quad (8)$$

with $u_2(t_1; t_2) = u_1(t_1) u_1(t_2)$. Finally, $q_k^i = \kappa^i \delta^i - b^i (t_{k+1}^i - t_k^i)$.

Proof: The relationship (7) follows by replacing the functional form of $v^i(t)$ given in (5) in equation (6) above. \square

Remark 2. $u_2(t_1, t_2) = u_1(t_1) \cdot u_1(t_2)$ can be interpreted as a nonlinear map of the stimulus u_1 into u_2 defined in a higher dimensional space. The operation performed by the second order Volterra kernel on u_2 in (8) is linear. Thus, (7) shows that the encoding of temporal stimuli can be viewed as generalized sampling [18].

The above formalism for encoding stimuli with complex cells can be extended in several ways. First, conductance-based BSGs such as the Hodgkin-Huxley and Morris-Lecar neuron models, and Izhikevich point neuron models can be employed [25, 26, 27, 28]. The encoding can be similarly formulated as generalized sampling [16]. Second, to capture the stochastic nature of spiking neurons intrinsic noise can be added into the BSG models. For example, an IAF neuron with random thresholds can be used [29, 15]. It is also natural to consider intrinsic noise in the conductance-based BSGs [19]. For both models, it has been shown that the encoding of stimuli can be viewed as *generalized sampling with noisy measurements* [15, 19], i.e., the t-transform is of the form

$$\mathcal{T}_k^i u_2 = q_k^i + \varepsilon_k^i, k \in \mathbb{I}^i, i = 1, \dots, M, \quad (9)$$

where \mathcal{T}_k^i are bounded linear functionals defined according to the neuron model of choice, and ε_k^i represents random noise in the measurements.

In what follows, we will mainly focus on encoding circuits consisting of complex cells whose spiking mechanism is modeled by a deterministic IAF neuron. The results obtained can be extended to the above two cases, and we will provide examples for both of these.

2.3 Decoding of Temporal Stimuli Encoded by a Population of Complex Cells

Assuming that the spike times $(t_k^i), k \in \mathbb{I}^i, i = 1, 2, \dots, M$, are known, by Lemma 1, the neural circuit with complex cells encodes the stimulus via a set of linear functionals acting on u_2 (see equation (7)). Thus, the reconstruction of u_2 can *in principle* be obtained by inverting the set of linear equations (7) [18].

Theorem 1. *The coefficients of $u_2 \in \mathcal{H}_2$ in (2) satisfy the following system of linear equations*

$$\Xi \mathbf{d} = \mathbf{q}, \quad \text{where} \quad \Xi = [(\Xi^1)^T, \dots, (\Xi^M)^T]^T \quad \text{and} \quad \mathbf{q} = [(\mathbf{q}^1)^T, \dots, (\mathbf{q}^M)^T]^T \quad (10)$$

with $[\mathbf{q}^i]_k = q_k^i$, $[\mathbf{d}]_{l_{t_1} l_{t_2}} = d_{l_{t_1} l_{t_2}}$ and

$$[\Xi^i]_{k; l_{t_1} l_{t_2}} = \int_{t_k^i}^{t_{k+1}} e_{l_{t_1} + l_{t_2}}(t) dt \int_{\mathbb{D}^2} h_2^i(s_1; s_2) e_{-l_{t_1}}(s_1) e_{-l_{t_2}}(s_2) ds_1 ds_2.$$

The above result can be obtained by plugging (2) into (7). We refer readers to Theorem 1 in [18] for a detailed proof.

We formulate the reconstruction of u_2 as the following optimization problem:

$$\hat{u}_2(t_1; t_2) = \operatorname{argmin}_{u_2 \in \mathcal{H}_2} \sum_{i=1}^M \sum_{k \in \mathbb{I}^i} (\mathcal{T}_k^i u_2 - q_k^i)^2. \quad (11)$$

Algorithm 1. *The solution to (11) is given by*

$$\hat{u}_2(t_1; t_2) = \sum_{l_{t_1}=-L_t}^{L_t} \sum_{l_{t_2}=-L_t}^{L_t} \hat{d}_{l_{t_1} l_{t_2}} e_{l_{t_1}}(t_1) \cdot e_{l_{t_2}}(t_2), \quad (12)$$

where $\hat{\mathbf{d}} = [\hat{d}_{-L_t, -L_t}, \dots, \hat{d}_{-L_t, L_t}, \dots, \dots, \hat{d}_{L_t, -L_t}, \dots, \hat{d}_{L_t, L_t}]^T$ is obtained by

$$\hat{\mathbf{d}} = \Xi^\dagger \mathbf{q} \quad (13)$$

with † denoting the pseudoinverse operator.

We note that a necessary condition for perfect recovery is that the total number of spikes exceeds $\dim(\mathcal{H}_1)(\dim(\mathcal{H}_1) + 1)/2 + M$ [19]. Therefore, the complexity of the decoding algorithm is on the order of $\dim(\mathcal{H}_1)^2$.

Following [18, 19], the decoding algorithm is called a Volterra Time Decoding Machine (Volterra TDM).

2.4 Functional Identification of DSPs of Complex Cells

In this section, we formulate the functional identification of a single complex cell in the neural circuit described in Figure 2A. We perform M experimental trials. In trial i , $i = 1, \dots, M$, we present a controlled stimulus $u_1^i(t)$ to the cell and observe the spike times $(t_k^i)_{k \in \mathbb{I}^i}$. We assume the cell has a DSP of the form $h_2(t_1; t_2) = g_1^1(t_1)g_1^1(t_2) + g_1^2(t_1)g_1^2(t_2)$ and an integrate and fire BSG with integration constant, bias and threshold denoted by κ, b and δ , respectively. The objective is to functionally identify h_2 from the knowledge of u_1^i and the observed spikes $(t_k^i)_{k \in \mathbb{I}^i}$, $i = 1, \dots, M$. This is a standard practice in neurophysiology for inferring the functional form of a component of a sensory system [1].

Definition 3. Let $h_p \in \mathbb{L}^1(\mathbb{D}^p)$, $p = 1, 2$, where \mathbb{L}^1 denotes the space of Lebesgue integrable functions. The operator $\mathcal{P}_1 : \mathbb{L}_1(\mathbb{D}) \rightarrow \mathcal{H}_1$ given by

$$(\mathcal{P}_1 h_1)(t) = \int_{\mathbb{D}} h_1(t') K_1(t; t') dt' \quad (14)$$

is called the projection operator from $\mathbb{L}^1(\mathbb{D})$ to \mathcal{H}_1 . Similarly, the operator $\mathcal{P}_2 : \mathbb{L}_1(\mathbb{D}^2) \rightarrow \mathcal{H}_2$ is given by

$$(\mathcal{P}_2 h_2)(t_1; t_2) = \int_{\mathbb{D}^2} h_2(t'_1; t'_2) K_2(t_1, t_2; t'_1, t'_2) dt'_1 dt'_2 \quad (15)$$

is called the projection operator from $\mathbb{L}^1(\mathbb{D}^2)$ to \mathcal{H}_2 .

Note, that for $u_1^i \in \mathcal{H}_1$, $\mathcal{P}_1 u_1^i = u_1^i$. Moreover, with $u_2^i(t_1, t_2) = u_1^i(t_1)u_1^i(t_2)$, $\mathcal{P}_2 u_2^i = u_2^i$.

Lemma 2. With M trials of stimuli $u_2^i(t_1; t_2) = u_1^i(t_1)u_1^i(t_2)$, $i = 1, \dots, M$, presented to a complex cell having DSP $h_2(t_1, t_2)$, we have

$$\mathcal{L}_k^i(\mathcal{P}_2 h_2) = q_k^i, k \in \mathbb{I}^i, i = 1, \dots, M, \quad (16)$$

where

$$\mathcal{L}_k^i(\mathcal{P}_2 h_2) = \int_{t_k^i}^{t_{k+1}^i} \int_{\mathbb{D}^2} u_2^i(t - s_1; t - s_2) (\mathcal{P}_2 h_2)(t - s_1; t - s_2) ds_1 ds_2 dt, \quad (17)$$

and

$$q_k^i = \kappa^i \delta^i - b^i (t_{k+1}^i - t_k^i). \quad (18)$$

Proof: Proof can be found in Appendix A.

Remark 3. The similarity between equations (7) and (72) suggests that the identification of a complex cell DSP by presenting multiple stimuli is dual to decoding a stimulus encoded by a population of complex cells. This duality is schematically shown in Figure 3.

Theorem 2. Let $\mathcal{P}_2 h_2 \in \mathcal{H}_2$ be of the form

$$\mathcal{P}_2 h_2(t_1; t_2) = \sum_{l_{t_1}=-L_t}^{L_t} \sum_{l_{t_2}=-L_t}^{L_t} h_{l_{t_1} l_{t_2}} e_{l_{t_1}}(t_1) \cdot e_{l_{t_2}}(t_2). \quad (19)$$

Then, $[\mathbf{h}]_{l_{t_1} l_{t_2}} = h_{l_{t_1} l_{t_2}}$ with $l_{t_1} = -L_t, \dots, L_t$, $l_{t_2} = -L_t, \dots, L_t$, satisfies the following system of linear equations

$$\Theta \mathbf{h} = \mathbf{q}, \quad (20)$$

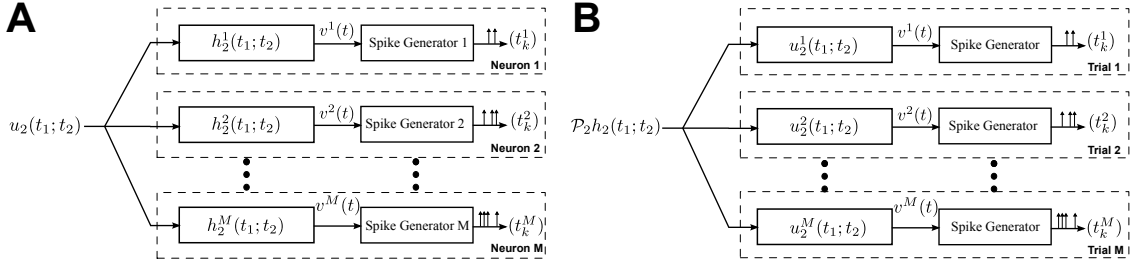


Figure 3: Duality between decoding and identification. (A) The stimulus $u_1(t)$ is encoded with a population of complex cells. (B) The projection of the second-order Volterra DSP of an arbitrary neuron on the input space generates the same spike trains if the impulse responses of the DSPs are the same as the input stimuli in repeated trials.

where $\Theta = [(\Theta^1)^T, \dots, (\Theta^M)^T]^T$ and $\mathbf{q} = [(\mathbf{q}^1)^T, \dots, (\mathbf{q}^M)^T]^T$ with $[\mathbf{q}^i]_k = q_k^i$, and

$$[\Theta^i]_{k; l_{t_1} l_{t_2}} = \int_{t_k^i}^{t_{k+1}} e_{l_{t_1} + l_{t_2}}(t) dt \int_{\mathbb{D}^2} u_2^i(s_1; s_2) e_{-l_{t_1}}(s_1) e_{-l_{t_2}}(s_2) ds_1 ds_2. \quad (21)$$

Thus, to identify $\mathcal{P}_2 h_2$, we can follow the same methodology as in Algorithm 1, and formulate the functional identification of $\mathcal{P}_2 h_2$ as

$$\widehat{\mathcal{P}_2 h_2} = \operatorname{argmin}_{\mathcal{P}_2 h_2 \in \mathcal{H}_2} \sum_{i=1}^M \sum_{k \in \mathbb{I}^i} (\mathcal{L}_k^i(\mathcal{P}_2 h_2) - q_k^i)^2. \quad (22)$$

For a detailed proof we refer the reader to the proof of Theorem 1 in [18].

Algorithm 2. *The solution to (22) is given by*

$$\widehat{\mathcal{P}_2 h_2}(t_1; t_2) = \sum_{l_{t_1}=-L_t}^{L_t} \sum_{l_{t_2}=-L_t}^{L_t} \hat{h}_{l_{t_1} l_{t_2}} e_{l_{t_1}}(t_1) \cdot e_{l_{t_2}}(t_2), \quad (23)$$

where $\hat{\mathbf{h}} = [\hat{h}_{-L_t, -L_t}, \dots, \hat{h}_{-L_t, L_t}, \dots, \dots, \hat{h}_{L_t, -L_t}, \dots, \hat{h}_{L_t, L_t}]^T$ is obtained by

$$\hat{\mathbf{h}} = \Theta^\dagger \mathbf{q}. \quad (24)$$

The methodology described in Algorithm 2 to identify the nonlinear DSP is called the Volterra Channel Identification Machine (Volterra CIM) [18, 19].

Remark 4. *Formulating the decoding and identification problems in the tensor product space \mathcal{H}_2 allows the identification of nonlinear processing by solving a set of linear equations. However, due to the increased dimensionality, the algorithm requires for decoding $\mathcal{O}(\dim(\mathcal{H}_1)^2)$ measurements.*

3 Low-Rank Decoding and Functional Identification

As shown in Section 2.3, a reconstruction of the signal u_2 is in principle possible by solving a set of linear equations. However, the complexity of the algorithm is prohibitive. We show

in this section that an efficient decoding algorithm can be constructed that exploits the structure of encoding circuits with complex cells. Based on the duality between decoding and functional identification, functional identification algorithms that exploit the structure of the DSP of complex cells are presented. These algorithms largely reduce the complexity of decoding of temporal stimuli encoded by an ensemble of complex cells and that of functional identification of their DSPs.

3.1 Low-Rank Decoding of Stimuli

3.1.1 Exploiting the Structure of Complex Cell Encoding

In Theorem 1, we introduced a vector notation for the coefficients of u_2

$$\mathbf{d} = [d_{-L_t, -L_t}, \dots, d_{-L_t, L_t}, \dots, \dots, d_{L_t, -L_t}, \dots, d_{L_t, L_t}]^T. \quad (25)$$

We introduce here the matrix notation of the coefficients for $u_2 \in \mathcal{H}_2$,

$$\mathbf{D} = \begin{bmatrix} d_{-L_t, L_t} & \dots & d_{-L_t, -L_t} \\ \vdots & \ddots & \vdots \\ d_{L_t, L_t} & \dots & d_{L_t, -L_t} \end{bmatrix}. \quad (26)$$

We notice the following: i) since u_2 is assumed to be real, $\overline{d_{l_{t_1}, l_{t_2}}} = d_{-l_{t_1}, -l_{t_2}}$, and ii) since $u_2(t_1; t_2) = u_1(t_1)u_1(t_2) = u_1(t_2)u_1(t_1) = u_2(t_2; t_1)$, we have $d_{l_{t_1}, l_{t_2}} = d_{l_{t_2}, l_{t_1}}$. These properties imply that \mathbf{D} is a Hermitian matrix. Moreover, we note that u_2 in (7) is the “outer” product of the stimuli u_1 , *i.e.*,

$$\mathbf{D} = \mathbf{c}\mathbf{c}^H, \quad (27)$$

where

$$\mathbf{c} = [c_{-L_t}, \dots, c_{L_t}]^T \quad (28)$$

are the coefficients of the basis functions of u_1 . Therefore, \mathbf{D} is a rank-1 Hermitian positive semidefinite matrix. This property will be exploited in stimulus decoding (reconstruction).

Theorem 3. *Encoding the stimulus $u_1 \in \mathcal{H}_1$ with the neural circuit with complex cells given in (6) into the spike train sequence $(t_k^i), k \in \mathbb{I}^i, i = 1, 2, \dots, M$, satisfies the set of equations*

$$\text{Tr}(\Phi_k^i \mathbf{D}) = q_k^i, k \in \mathbb{I}^i, i = 1, \dots, M, \quad (29)$$

where $\text{Tr}(\cdot)$ is the trace operator, \mathbf{D} is the rank-1 positive semidefinite Hermitian matrix $\mathbf{D} = \mathbf{c}\mathbf{c}^H$, $q_k^i = \kappa^i \delta^i - b^i (t_{k+1}^i - t_k^i)$ and $(\Phi_k^i), k \in \mathbb{I}^i, i = 1, \dots, M$, are Hermitian matrices with entries in the $(l_{t_2} + L_t + 1)$ -th row and $(l_{t_1} + L_t + 1)$ -th column given by

$$[\Phi_k^i]_{l_{t_2}, l_{t_1}} = \int_{t_k^i}^{t_{k+1}^i} e_{l_{t_1} - l_{t_2}}(t) dt \int_{\mathbb{D}^2} h_2^i(s_1; s_2) e_{-l_{t_1}}(s_1) e_{l_{t_2}}(s_2) ds_1 ds_2. \quad (30)$$

Proof: Plugging in the general form of u_2 in (2) into (8), the left hand side of (7) amounts to

$$\sum_{l_{t_1}=-L_t}^{L_t} \sum_{l_{t_2}=-L_t}^{L_t} d_{l_{t_1}, -l_{t_2}} \int_{t_k^i}^{t_{k+1}^i} e_{l_{t_1} - l_{t_2}}(t) dt \int_{\mathbb{D}^2} h_2^i(s_1; s_2) e_{-l_{t_1}}(s_1) e_{l_{t_2}}(s_2) ds_1 ds_2.$$

It is easy to verify that the above expression can be written as

$$\sum_{l_{t_1}=-L_t}^{L_t} \sum_{l_{t_2}=-L_t}^{L_t} d_{l_{t_1}, -l_{t_2}} [\Phi_k^i]_{l_{t_2}, l_{t_1}} = \text{Tr}(\Phi_k^i \mathbf{D}). \quad (31)$$

Finally, we note that since $h_2^i, i = 1, \dots, M$, are assumed to be real valued, $(\Phi_k^i), k \in \mathbb{I}^i, i = 1, \dots, M$, are Hermitian. \square

Remark 5. We note that equation (29) in Theorem 3 and equation (10) in Theorem 1 are the same. These equations represent the t-transform of a complex cell in (rank-1) matrix and vector form, respectively. The (rank-1) matrix representation is made possible by the equality $u_2(t_1; t_2) = u_1(t_1)u_1(t_2)$.

3.1.2 Reconstruction Algorithms

Solving the systems of equations (29) and (10) requires at least $\dim(\mathcal{H}_1)(\dim(\mathcal{H}_1)+1)/2 + M$ measurements. Consequently, practical solutions become quickly intractable. Fortunately, the encoded stimulus is of the form $u_2(t_1; t_2) = u_1(t_1)u_1(t_2)$. This guarantees that \mathbf{D} is a rank-1 matrix and thus the reconstructed stimulus belongs to a small subset of \mathcal{H}_2 . Therefore, we can cast the problem of reconstructing temporal stimuli encoded by neural circuits with complex cells as a feasibility problem, that is, find all positive semidefinite Hermitian matrices that satisfy (29) and have rank 1. As we shall demonstrate, the latter condition can be satisfied with substantially fewer measurements.

Recently, there is an increasing interest in low-rank optimizations such as matrix factorization, matrix completion and rank minimization, both from a theoretical and from a practical standpoint [30, 23, 31]. For example, rank minimization has recently been applied to phase retrieval problems [21].

Our objective here is to find rank-1, positive-semidefinite matrices that satisfy the t-transform (29). Since there always exists at least one rank-1 solution, this is equivalent to the following optimization problem [32]

$$\begin{aligned} & \text{minimize} && \text{Rank}(\mathbf{D}) \\ & \text{s.t.} && \text{Tr}(\Phi_k^i \mathbf{D}) = q_k^i, k \in \mathbb{I}^i, i = 1, \dots, M, \\ & && \mathbf{D} \succcurlyeq 0 \end{aligned} \quad (32)$$

The rank minimization problem in (32) is NP-hard. A well known heuristic is to relax the problem (32) to a trace minimization problem [31]. That is, instead of solving (32), we reconstruct u_2 using Algorithm 3.

Algorithm 3. The reconstruction of u_2 from the spike times generated by the neural circuit with complex cells is given by

$$\hat{u}_2(t_1; t_2) = \sum_{l_{t_1}=-L_t}^{L_t} \sum_{l_{t_2}=-L_t}^{L_t} \hat{d}_{l_{t_1} l_{t_2}} e_{l_{t_1}}(t_1) \cdot e_{l_{t_2}}(t_2), \quad (33)$$

where

$$\hat{\mathbf{D}} = \begin{bmatrix} \hat{d}_{-L_t, L_t} & \dots & \hat{d}_{-L_t, -L_t} \\ \vdots & \ddots & \vdots \\ \hat{d}_{L_t, L_t} & \dots & \hat{d}_{L_t, -L_t} \end{bmatrix}. \quad (34)$$

is the solution to the semidefinite programming (SDP) problem

$$\begin{aligned} & \text{minimize} && \text{Tr}(\mathbf{D}) \\ & \text{s.t.} && \text{Tr}(\Phi_k^i \mathbf{D}) = q_k^i, k \in \mathbb{I}^i, i = 1, \dots, M, \\ & && \mathbf{D} \succcurlyeq 0 \end{aligned} \quad (35)$$

When the matrices (Φ_k^i) , $k \in \mathbb{I}^i$, $i = 1, \dots, M$, satisfy the rank restricted isometry property [23], the trace norm relaxation converges to the true solution of (32) provided that the number of measurements is of the order $\mathcal{O}\left(\dim(\mathcal{H}_1)\log(\dim(\mathcal{H}_1))\right)$ [23]. These results suggest that stimuli encoded by complex cells can be decoded with a significantly lower number of measurements than that required by Algorithm 1. To investigate this further, we applied the above algorithm to decode a large number of stimuli encoded by complex cells while varying the number of measurements (spikes) used by the decoding algorithm. The results show that the number of spikes required to faithfully represent a stimulus by a neural circuits consisting of complex cells is quasilinearly rather than quadratically proportional to the dimension of the stimulus space. These results are presented in the subsequent sections.

The matrix of weights $\hat{\mathbf{D}}$ obtained from the above algorithm can be further decomposed to extract the signal u_1 (up to a sign) as follows.

- (i) Perform the eigen-decomposition of $\hat{\mathbf{D}}$. Denote the largest eigenvalue by λ and the corresponding eigenvector by \mathbf{v} . If (35) does not exactly return a rank-1 matrix, choose the largest eigenvalue and disregard the rest. Let $\mathbf{w} = \sqrt{\lambda}\mathbf{v}$.
- (ii) The reconstructed stimulus \hat{u}_1 is given by (up to a sign)

$$\hat{u}_1(t) = \sum_{l_t=-L_t}^{L_t} \hat{c}_{l_t} e_{l_t}(t),$$

where

$$\hat{\mathbf{c}} = \begin{cases} \mathbf{w} \cdot \frac{[\mathbf{w}]_{L_t+1}}{[\mathbf{w}]_{L_t+1}}, & \text{if } [\mathbf{w}]_{L_t+1} \neq 0 \\ \mathbf{w}, & \text{otherwise} \end{cases} \quad (36)$$

with $\hat{\mathbf{c}} = [\hat{c}_{-L_t}, \dots, \hat{c}_{L_t}]^T$, and $[\mathbf{w}]_{L_t+1}$ is the $(L_t + 1)^{\text{th}}$ entry of \mathbf{w} , which corresponds to the coefficient \hat{c}_0 .

If $\hat{\mathbf{D}}$ is rank 1, step (i) decomposes $\hat{\mathbf{D}}$ as an “outer” product of a vector and itself (see (27)). The resulting vector \mathbf{w} differs from the actual coefficient vector of the stimulus u_1 by up to a complex-valued scaling factor. This factor is corrected in step (ii). Since u_1 is assumed to be real-valued, the “DC” component must be real-valued. Therefore, we rotate \mathbf{w} to remove any imaginary part. In practice, this also ensures $\hat{c}_{-l_t} = \overline{\hat{c}_{l_t}}$.

Remark 6. Note that we can reconstruct $u_1(t)$ up to a sign, since $\mathbf{D} = \mathbf{cc}^H$ and $\mathbf{D} = (-\mathbf{c})(-\mathbf{c}^H)$ are equally possible. For clarity, in all examples given in this paper, the sign of the recovered stimulus was matched to the original stimulus.

Remark 7. Note that (32) can be alternatively solved by replacing the objective with the log-det heuristic [31], that is

$$\begin{aligned} & \text{minimize} && \log \det(\mathbf{D} + \lambda \mathbf{I}) \\ & \text{s.t.} && \mathbf{Tr}(\Phi_k^i \mathbf{D}) = q_k^i, k \in \mathbb{I}^i, i = 1, \dots, M, \\ & && \mathbf{D} \succcurlyeq 0 \end{aligned} \quad (37)$$

where $\lambda > 0$ is a small regularization constant. This optimization may further reduce the rank of $\hat{\mathbf{D}}$ when Algorithm 3 fails to progress to an exact rank-1 solution [31].

Remark 8. When intrinsic noise is present in the BSG, the encoding of stimuli can be formulated as generalized sampling with noisy measurements. We modify (35) as follows

$$\begin{aligned} & \text{minimize} && \mathbf{Tr}(\mathbf{D}) + \lambda \left(\sum_{i=1}^M \sum_{k \in \mathbb{I}^i} (\mathbf{Tr}(\Phi_k^i \mathbf{D}) - q_k^i)^2 \right), \\ & \text{s.t.} && \mathbf{D} \succcurlyeq 0 \end{aligned} \quad (38)$$

where λ can be chosen based on the noise estimate. Here, the recovered \mathbf{D} may not longer be rank-1. The largest rank-1 component is used for the reconstruction of stimuli.

While the SDP in (35) provides an elegant way for relaxing the rank minimization problem, it is limited in practice by the need of large amounts of computer memory for numerical calculations. The optimization problem (32) can also be solved using an alternating minimization scheme [33] as outlined in Algorithm 4 below. The alternating minimization approach is more tractable when the dimension of the space is very large. Algorithm 4 uses an initialization step (step 1 below) that provides an initial iterate whose distance from \mathbf{D} is bounded. It then alternately solves for the left and right singular vector of the rank-1 matrix \mathbf{D} while keeping the other one fixed (step 2 below). The resulting subproblems admit a straightforward least squares solution, that can be much more efficiently solved than the SDP in Algorithm 3. Moreover, the algorithm is amenable to parallel computation using General Purpose Graphics Processing Units (GPGPUs). The latter property makes it even more attractive when the dimension of the stimulus space is large.

Algorithm 4. 1. Initialize $\hat{\mathbf{c}}_1$ and $\hat{\mathbf{c}}_2$ to top left and right singular vector respectively of $\sum_{i=1}^M \sum_{k \in \mathbb{I}^i} q_k^i \Phi_k^i$ normalized to $\sqrt{\frac{1}{\sigma} \sum_{i=1}^M \sum_{k \in \mathbb{I}^i} (q_k^i)^2}$, where σ is the top singular value of $\sum_{i=1}^M \sum_{k \in \mathbb{I}^i} q_k^i \Phi_k^i$.
2. Solve alternately the following two minimization problems

(a) solve for $\hat{\mathbf{c}}_1$ by fixing $\hat{\mathbf{c}}_2$

$$\hat{\mathbf{c}}_1 = \min_{\mathbf{c}_1} \sum_{i=1}^M \sum_{k \in \mathbb{I}^i} (\mathbf{Tr}(\Phi_k^i \mathbf{c}_1 \hat{\mathbf{c}}_2^H) - q_k^i)^2 \quad (39)$$

(b) solve for $\hat{\mathbf{c}}_2$ by fixing $\hat{\mathbf{c}}_1$

$$\hat{\mathbf{c}}_2 = \min_{\mathbf{c}_2} \sum_{i=1}^M \sum_{k \in \mathbb{I}^i} (\text{Tr}(\Phi_k^i \hat{\mathbf{c}}_1 \mathbf{c}_2^H) - q_k^i)^2 \quad (40)$$

until $\sum_{i=1}^M \sum_{k \in \mathbb{I}^i} (\text{Tr}(\Phi_k^i \hat{\mathbf{c}}_1 \hat{\mathbf{c}}_2^H) - q_k^i)^2 \leq \epsilon$, where $\epsilon > 0$ is the error tolerance level.

3. compute $\hat{\mathbf{D}} = \hat{\mathbf{c}}_1 \hat{\mathbf{c}}_2^H$.

$\hat{\mathbf{D}}$ approximates the coefficients of $u_2 \in \mathcal{H}_2$ as in (33). We can reconstruct u_1 , using the (appropriately scaled) top eigenvector of $\frac{1}{2}(\hat{\mathbf{D}} + \hat{\mathbf{D}}^H)$. This can be obtained directly from $\hat{\mathbf{c}}_1$ and $\hat{\mathbf{c}}_2$ as follows. Let

$$k = \frac{\hat{\mathbf{c}}_1^H \hat{\mathbf{c}}_2 - \hat{\mathbf{c}}_2^H \hat{\mathbf{c}}_1 + \sqrt{(\hat{\mathbf{c}}_1^H \hat{\mathbf{c}}_2 - \hat{\mathbf{c}}_2^H \hat{\mathbf{c}}_1)^2 + 4\hat{\mathbf{c}}_1^H \hat{\mathbf{c}}_1 \hat{\mathbf{c}}_2^H \hat{\mathbf{c}}_2}}{2\hat{\mathbf{c}}_2^H \hat{\mathbf{c}}_2}, \quad (41)$$

and

$$\mathbf{w} = \sqrt{\frac{1}{2}\hat{\mathbf{c}}_2^H \hat{\mathbf{c}}_1 + k\hat{\mathbf{c}}_2^H \hat{\mathbf{c}}_2} \frac{\hat{\mathbf{c}}_1 + k\hat{\mathbf{c}}_2}{\|\hat{\mathbf{c}}_1 + k\hat{\mathbf{c}}_2\|}, \quad (42)$$

the reconstructed stimulus \hat{u}_1 is given by (up to a sign)

$$\hat{u}_1(t) = \sum_{l_t=-L_t}^{L_t} \hat{c}_{l_t} e_{l_t}(t),$$

with $\hat{\mathbf{c}}$ given by Equation (36).

We point out that we made the decoding manageable by exploiting the structure of u_2 . Therefore, there is no constraint on the exact form $h_2^i(t_1; t_2)$ can take, and the decoding algorithms can be applied to neural circuits with neurons whose DSPs take the form of any second-order Volterra kernel.

3.1.3 Example - Decoding of Temporal Stimuli Encoded with a Population of Complex Cells

Here, the neural circuit we consider consists of 19 complex cells. The DSPs of the complex cells are of the form

$$h_2^i(t_1; t_2) = g_1^{i1}(t_1)g_1^{i1}(t_2) + g_1^{i2}(t_1)g_1^{i2}(t_2), \quad (43)$$

where $g_1^{i1}(t)$ and $g_1^{i2}(t)$ are quadrature pairs of temporal Gabor filters and $i = 1, \dots, 19$. The Gabor filters are constructed using a dyadic grid of dilations and translations of the mother wavelets. The mother functions are given by

$$g_1^1(t) = \exp\left(-\left(\frac{t^2}{0.001}\right)\right) \cos(40\pi t), \quad (44)$$

and

$$g_1^2(t) = \exp\left(-\left(\frac{t^2}{0.001}\right)\right) \sin(40\pi t). \quad (45)$$

The ensemble of Gabor filters spans the frequency range of the input space. The BSG of the complex cells are point IAF neurons with bias $b^i = 2$ and integration constant $\kappa^i = 1$, for $i = 1, \dots, M$. These two parameters are kept the same for all stimuli. Different threshold values are chosen for the IAF neurons in order to vary the total number of spikes, which can be used to evaluate how many measurements are required for perfectly reconstructing the input stimuli.

The domain of the input space \mathcal{H}_1 is $\mathbb{D} = [0, 1]$ (sec) and $L_t = 20, \Omega_t = 20 \cdot 2\pi$ (rad/sec). Thus, we have $\dim(\mathcal{H}_1) = 41$. The stimuli were generated by randomly choosing their basis coefficients from an i.i.d. Gaussian distribution.

We tested the encoding and subsequent decoding of 6,570 stimuli. The total number of spikes produced for each stimulus ranged from 20 to 220. Reconstructions of the stimuli were performed using Algorithm 3, and the SDPs were solved using SDPT3 [34].

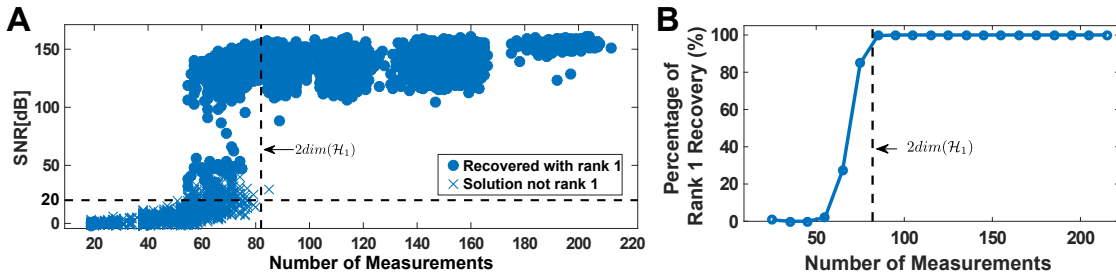


Figure 4: Example of low-rank decoding. (A) Effect of number of measurements (spikes) on reconstruction quality. (B) Percentage of rank 1 reconstructions.

We show the SNR of all reconstructions in the scatter plot of Figure 4A. Here solid dots represent exact rank 1 solutions (largest eigenvalue is at least 100 times larger than the sum of the rest of the eigenvalues), and crosses indicate that the trace minimization found a higher rank solution that has a smaller trace. The percentage of exact rank 1 solutions is shown in Figure 4B. A relatively sharp transition from very low probability of recovery to very high rate of perfect reconstruction can be seen, similar to phase transition phenomena in other sparse recovery algorithms [35]. It can also be seen that the number of measurements that are needed for perfect recovery is substantially lower than the 861 spikes required by decoding based on Theorem 1.

3.1.4 Example - IAF Spike Generators with Random Thresholds

Next, for the circuit presented in Section 3.1.3, we assumed the IAF neurons to have random thresholds [15]. More specifically, during the interval $[t_k^i, t_{k+1}^i)$ the threshold of the i^{th} neuron was δ_k^i . δ_k^i are i.i.d Gaussian random variables with mean δ and variance σ^2 . Since the thresholds are random, the spike times generated by the circuit are no longer deterministic.

We chose five different values for δ and four different values for σ . For each (δ, σ) pair, we presented 50 stimuli to the circuit and subsequently decoded these by solving (38). We found that the SNR of the recovery degrades linearly with $\log(\sigma)$. Figure 5 depicts the average SNR of recovery as a function of σ for various δ . Note that a lower δ corresponds to a higher number of spikes; the inset in the figure provides the average number of spikes produced by the circuit for each δ . The results demonstrate that the low-rank decoding algorithm is stable to noise and applicable to non-deterministic encoding paradigms.

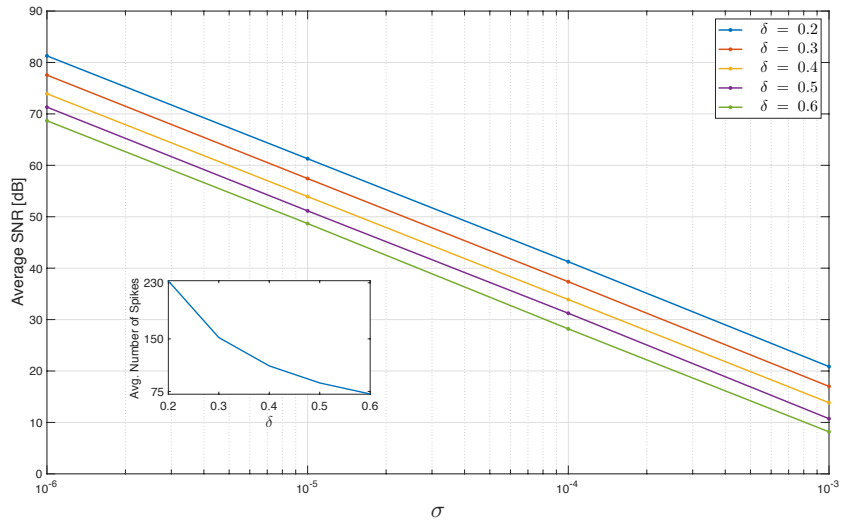


Figure 5: Robust reconstruction of temporal stimuli encoded by complex cells. The BSGs of the complex cells are modeled as ideal IAF neurons with random thresholds. The thresholds of the IAF neurons were independently drawn from $\mathcal{N}(\delta, \sigma^2)$. The inset shows the average number of spikes generated by the entire circuit for each choice of the threshold δ .

3.1.5 Example - Hodgkin-Huxley Neurons as Biophysical Spike Generators

Here, we evaluate the decoding of stimuli encoded by complex cells with BSGs modeled as Hodgkin-Huxley neurons. The space of the input stimuli and the structure of the DSPs of the neurons is the same as in Sections 3.1.3 and 3.1.4. However, as the Hodgkin-Huxley point neurons generate significantly more spikes than the IAF neurons considered in the previous examples, we only use here a total of 5 neurons. Again, the DSPs of these 5 neurons span the frequency range of the input space. We presented the circuit with 1,000 stimuli and subsequently performed their sparse decoding. The average number of spikes generated by the circuit across all stimuli was 215. Figure 6 shows the histogram of the SNRs of the decoded stimuli, with the insets depicting the original and decoded waveforms of a few representative stimuli. These results demonstrate that the low-rank decoding framework presented in this section can also be applied to stimuli encoded with a wide range of spike generators, including the biophysically realistic conductance-based models.

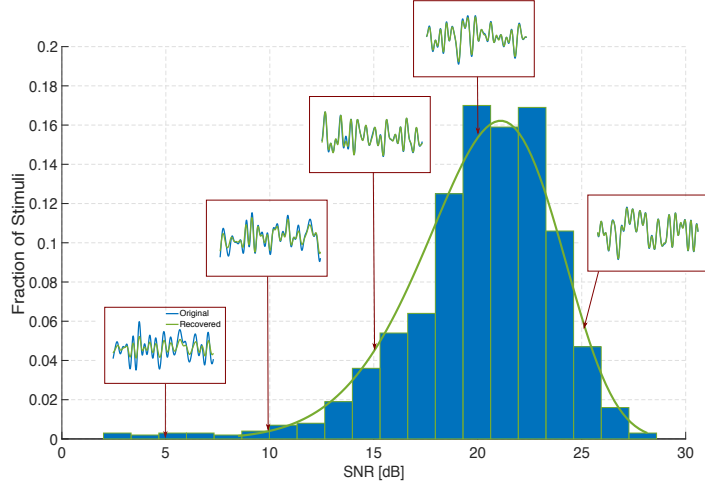


Figure 6: Histogram of reconstruction SNRs of stimuli encoded by complex cells. The BSGs of the complex cells are modeled as Hodgkin-Huxley point neurons. Insets show the original (blue) and recovered (green) stimuli for various SNR values.

3.1.6 Example - Hodgkin-Huxley Neurons with Stochastic Ion Channels

Finally, we again consider the same circuit as in Section 3.1.5. However, intrinsic ion channel noise is added to the Hodgkin-Huxley point neurons. For a detailed mathematical treatment of Hodgkin-Huxley point neuron with stochastic ion channels, we refer the reader to [19]. Here, independent Brownian motion processes respectively drive each of the gating variables of the Hodgkin-Huxley neuron, i.e., n (activation of potassium channels), m (activation of sodium channels) and h (inactivation of sodium channels). The variance of the Brownian motion processes denoted by σ_1^2 , σ_2^2 and σ_3^2 , were respectively chosen to be, $10\sigma_1 = \sigma_2 = \sigma_3 = \sigma$. We presented 50 stimuli to the circuit and repeated the encoding for eight choices of σ . For each stimulus presentation, the spike times generated by the circuit were then utilized to recover the stimulus using the sparse reconstruction algorithm. The results are presented in Figure 7. The points in the figure correspond to the average SNR of the 50 reconstructions for each value of the chosen σ and the shaded area represents their standard deviation. As can be seen from the results, the low-rank decoding framework is robust to intrinsic noise in conductance-based spiking models up to a certain noise level.

3.2 Low-Rank Functional Identification of Complex Cells

3.2.1 Duality Between Low-Rank Functional Identification and Decoding

As discussed in Section 2.4, the complexity of identification using Algorithm 2 can be prohibitively high. Often, a very large number of stimulus presentation trials are required to fully identify the DSP of biological neurons. To mitigate this, we consider exploiting the structure of the DSP of complex cells as motivated by the tractability of the low rank decoding algorithm.

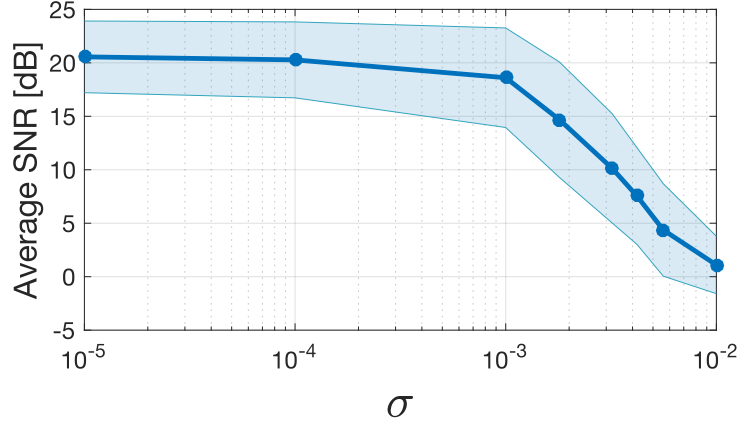


Figure 7: Robust reconstruction of stimuli encoded by complex cells with stochastic ion channels. The BSGs are modeled as Hodgkin-Huxley point neurons with stochastic ion channels. For each noise level σ , we set $10\sigma_1 = \sigma_2 = \sigma_3 = \sigma$ where $\sigma_i^2, i = 1, 2, 3$, are the variance of the independent Brownian motion process driving the gating variables n, m and h , respectively. A larger σ represents higher intrinsic noise strength.

We consider a single complex cell whose DSP is of the form

$$h_2(t_1; t_2) = \sum_{n=1}^N g_1^n(t_1)g_1^n(t_2), \quad (46)$$

where $g_1^n(t), n = 1, \dots, N$, are impulse responses of linear filters, and $N \ll \dim(\mathcal{H}_1)$. We note that a complex cell described in Figure 2A is a special case of (46) with $N = 2$. A natural question here is whether, by assuming such a structure, the functional identification of complex cell DSPs is tractable.

Remark 9. *It is well known that a second-order Volterra kernel has infinite equivalent forms but has a unique symmetric form [24].*

We have shown that the low-rank structure of u_2 leads to a reduction of complexity in the reconstruction of temporal stimuli encoded by an ensemble of complex cells. We also described the duality between decoding and functional identification. If we can show that the functional identification formalism for complex cell DSP is the dual to decoding of low-rank stimuli, it is straightforward to provide tractable algorithms for identifying $h_2(t_1; t_2)$ of the form (46).

Since $\mathcal{P}_1 g_1^n(t) \in \mathcal{H}_1, n = 1, \dots, N$, there is a set of coefficients $(g_{l_t}^n), l_t = -L_t, \dots, L_t$ and $n = 1, 2, \dots, N$, such that

$$\mathcal{P}_1 g_1^n(t) = \sum_{l_t=-L_t}^{L_t} g_{l_t}^n e_{l_t}(t). \quad (47)$$

In what follows we denote coefficients in vector form as

$$\mathbf{g}^n = [g_{-L_t}^n, \dots, g_{L_t}^n]^T. \quad (48)$$

Similarly, we denote the coefficients of $\mathcal{P}_1 h_2(t_1; t_2)$ in (19) in matrix form as

$$\mathbf{H} = \begin{bmatrix} h_{-L_t, L_t} & \dots & h_{-L_t, -L_t} \\ \vdots & \ddots & \vdots \\ h_{L_t, L_t} & \dots & h_{L_t, -L_t} \end{bmatrix}. \quad (49)$$

Then

$$\mathbf{H} = \sum_{n=1}^N \mathbf{g}^n (\mathbf{g}^n)^H \quad (50)$$

and thus \mathbf{H} is a Hermitian positive semidefinite matrix with rank at most N .

Theorem 4. *By presenting M trials of stimuli $u_2^i(t_1; t_2) = u_1^i(t_1)u_1^i(t_2)$, $i = 1, \dots, M$ to a complex cell, its coefficients satisfy the set of equations*

$$\text{Tr}(\Psi_k^i \mathbf{H}) = q_k^i, k \in \mathbb{I}^i, i = 1, \dots, M, \quad (51)$$

where $n_i + 1, i = 1, \dots, M$, is the number of spikes generated by the complex cell in trial i , \mathbf{H} is a Hermitian positive semidefinite matrix with $\text{rank}(\mathbf{H}) \leq N$, given by $\mathbf{H} = \sum_{n=1}^N \mathbf{g}^n (\mathbf{g}^n)^H$, with $\mathbf{g}^n = [g_{-L_t}^n, \dots, g_{L_t}^n]^T$, $(\Psi_k^i), k \in \mathbb{I}^i, i = 1, \dots, M$, are Hermitian matrices with entry at $(l_{t_2} + L_t + 1)$ -th row and $(l_{t_1} + L_t + 1)$ -th column given by

$$[\Psi_k^i]_{l_{t_2}; l_{t_1}} = \int_{t_k^i}^{t_{k+1}^i} e_{l_{t_1} - l_{t_2}}(t) dt \int_{\mathbb{D}^2} u_2^i(s_1; s_2) e_{-l_{t_1}}(s_1) e_{l_{t_2}}(s_2) ds_1 ds_2. \quad (52)$$

Proof: From Lemma 2, we have

$$\mathcal{L}_k^i(\mathcal{P}_2 h_2) = q_k^i, k \in \mathbb{I}^i, i = 1, \dots, M, \quad (53)$$

where

$$\mathcal{L}_k^i(\mathcal{P}_2 h_2) = \int_{t_k^i}^{t_{k+1}^i} \int_{\mathbb{D}^2} u_2^i(t - s_1; t - s_2) (\mathcal{P}_2 h_2)(s_1; s_2) ds_1 ds_2 dt. \quad (54)$$

(51) can be obtained following the steps of the proof of Theorem 3. \square

Remark 10. As in Section 3.2, we note that the similarity in (51) and (29) indicates the duality between low-rank functional identification of complex cells and low-rank decoding of stimuli encoded by a population of complex cells. The duality is illustrated in Figure 8.

3.2.2 Functional Identification Algorithms

To functionally identify the complex cell DSP, we again employ a rank minimization problem

$$\begin{aligned} & \text{minimize} && \text{Rank}(\mathbf{H}) \\ & \text{s.t.} && \text{Tr}(\Psi_k^i \mathbf{H}) = q_k^i, k \in \mathbb{I}^i, i = 1, \dots, M, \\ & && \mathbf{H} \succcurlyeq 0 \end{aligned} \quad (55)$$

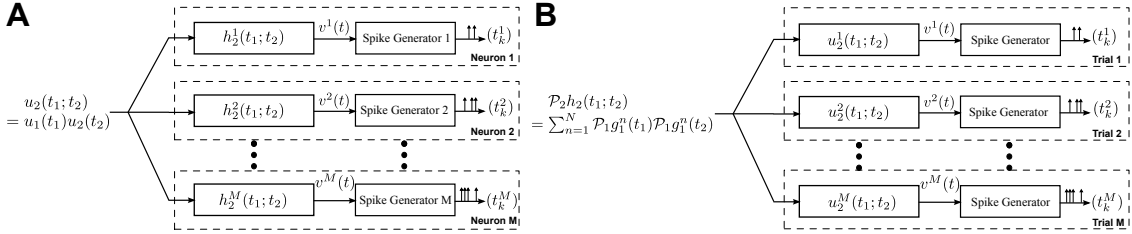


Figure 8: Duality between low-rank decoding and low-rank functional identification. Duality between low-rank decoding of a stimulus encoded by a population of complex cells and low-rank functional identification of complex cells. (A) The low-rank decoding algorithm assumes that the encoded stimulus can be written as $u_2(t_1; t_2) = u_1(t_1)u_2(t_2)$. (B) Functional identification of a complex cell assumes that the structure of the DSP is low rank, *i.e.*, $\mathcal{P}_2h_2(t_1; t_2) = \sum_{n=1}^N \mathcal{P}_1g_1^n(t_1)\mathcal{P}_1g_1^n(t_2)$.

Algorithm 3 provides a solution to the above rank minimization problem. However, in this case, the optimal solution shall have rank N . We relax the problem to a trace minimization problem and consider the following algorithm for low-rank functional identification of complex cells.

Algorithm 5. *The functional identification of complex cell DSP from the spike times generated by the neuron in M stimulus trials is given by*

$$\widehat{\mathcal{P}_2h_2}(t_1; t_2) = \sum_{l_{t_1}=-L_t}^{L_t} \sum_{l_{t_2}=-L_t}^{L_t} \hat{h}_{l_{t_1} l_{t_2}} e_{l_{t_1}}(t_1) \cdot e_{l_{t_2}}(t_2), \quad (56)$$

where

$$\hat{\mathbf{H}} = \begin{bmatrix} \hat{h}_{-L_t, L_t} & \dots & \hat{h}_{-L_t, -L_t} \\ \vdots & \ddots & \vdots \\ \hat{h}_{L_t, L_t} & \dots & \hat{h}_{L_t, -L_t} \end{bmatrix}. \quad (57)$$

is the solution to the SDP problem

$$\begin{aligned} & \text{minimize} && \text{Tr}(\mathbf{H}) \\ & \text{s.t.} && \text{Tr}(\Psi_k^i \mathbf{H}) = q_k^i, k \in \mathbb{I}^i, i = 1, \dots, M, \\ & && \mathbf{H} \succcurlyeq 0 \end{aligned} \quad (58)$$

Based on the results for decoding using Algorithm 3 and provided that h_2 is of the form (46), we intuitively inferred that the number of measurements for the perfect identification of \mathcal{P}_2h_2 is much smaller than $\mathcal{O}(\dim(\mathcal{H}_1)^2)$. We demonstrate that this is the case for a large number of identification examples in the subsequent sections.

This suggests that even if the dimension of the input space becomes large, the functional identification of the DSP of complex cells is still tractable. This result has critical implication for performing neurobiological experiments to functionally identify complex cells. First, it suggests that a much smaller number of stimulus trials is needed for perfect identification. Second, the total number of spikes/measurements that needs to be recorded can be significantly reduced. Both means the duration of experiment can be shortened.

Remark 11. Note that only the projection of the DSP h_2 onto the space of input stimuli can be identified.

Remark 12. We can use the largest N eigenvalues and their respective eigenvectors of $\hat{\mathbf{H}}$ to obtain the projection of individual linear filter components $\widehat{\mathcal{P}_1 g_1^n}$, $n = 1, \dots, N$. However, these components may not directly correspond to $\mathcal{P}_1 g_1^n$, $n = 1, \dots, N$, in that the original projections may not be “orthogonal”, whereas the eigenvalue decomposition imposes orthogonality.

As in Algorithm 4 when applied for solving the decoding problem, the rank minimization problem above can be solved using alternating minimization, as described in Algorithm 6 below. Here, we solve for the top N left and right singular vectors of \mathbf{H} alternately, where N is the rank of the second order Volterra DSP. We note that the initialization step is akin to running an algorithm very similar to the spike-triggered covariance (STC) algorithm widely used in neuroscience [36, 37, 38, 39, 40]. The subsequent steps then improve upon this initial estimate.

Algorithm 6. 1. Initialize $\hat{\mathbf{H}}_1$ and $\hat{\mathbf{H}}_2$ to top N left and right singular vectors, respectively, of $\sum_{i=1}^M \sum_{k=1}^{n_i} q_k^i \Psi_k^i$ with the n^{th} singular vector normalized to $\frac{1}{N} \sqrt{\frac{1}{\sigma_n} \sum_{i=1}^M \sum_{k=1}^{n_i} (q_k^i)^2}$, where σ_n is the top n^{th} singular value of $\sum_{i=1}^M \sum_{k=1}^{n_i} q_k^i \Psi_k^i$.

2. Solve the following two minimization problems

(a) solve for $\hat{\mathbf{H}}_1$ by fixing $\hat{\mathbf{H}}_2$

$$\hat{\mathbf{H}}_1 = \min_{\mathbf{H}_1 \in \mathbb{C}^{dim(\mathcal{H}_1) \times N}} \sum_{i=1}^M \sum_{k \in \mathbb{I}^i} (\text{Tr}(\Psi_k^i \mathbf{H}_1 \hat{\mathbf{H}}_2^H) - q_k^i)^2 \quad (59)$$

(b) solve for $\hat{\mathbf{H}}_2$ by fixing $\hat{\mathbf{H}}_1$

$$\hat{\mathbf{H}}_2 = \min_{\mathbf{H}_2 \in \mathbb{C}^{dim(\mathcal{H}_1) \times N}} \sum_{i=1}^M \sum_{k \in \mathbb{I}^i} (\text{Tr}(\Psi_k^i \hat{\mathbf{H}}_1 \mathbf{H}_2^H) - q_k^i)^2 \quad (60)$$

until $\sum_{i=1}^M \sum_{k \in \mathbb{I}^i} (\text{Tr}(\Psi_k^i \hat{\mathbf{H}}_1 \hat{\mathbf{H}}_2^H) - q_k^i)^2 \leq \epsilon$, where $\epsilon > 0$ is the error tolerance level.

3. compute $\hat{\mathbf{H}} = \frac{1}{2} (\hat{\mathbf{H}}_1 \hat{\mathbf{H}}_2^H + \hat{\mathbf{H}}_2 \hat{\mathbf{H}}_1^H)$.

3.2.3 Example - Identification of Complex Cell DSPs from Spike Times

In this example, we consider identifying a single complex cell having the following Volterra DSP

$$h_2(t_1, t_2) = g_1^1(t_1)g_1^1(t_1) + g_1^2(t_1)g_1^2(t_2), \quad (61)$$

where

$$g_1^1(t) = 50 \exp\left(-\frac{(t-0.3)^2}{0.002}\right) \cos(40\pi t), \quad (62)$$

$$g_1^2(t) = 50 \exp\left(-\frac{(t-0.3)^2}{0.002}\right) \sin(40\pi t). \quad (63)$$

In repeated trials we presented to the complex cell 1-second long stimuli chosen from the input space. The domain of the input space \mathcal{H}_1^1 is $\mathbb{D} = [0, 1]$ (sec) and $L_t = 20$, $\Omega_t = 20 \cdot 2\pi$ (rad/sec) and thus, $\dim(\mathcal{H}_1^1) = 41$. The stimuli were generated by independently choosing their basis coefficients from the same Gaussian distribution. We presented a total of 16,600 different stimuli in the repeated trials. We then randomly selected between 30-80 trial subsets such that the total number of spikes in each subset was between 60 and 160. We performed the identification process on each subset using Algorithm 5. The optimization problem was solved using SDPT3.

For each instantiation of the identification algorithm, we recorded whether the optimization process resulted in a rank-2 solution and also the SNR of the identified DSP with respect to the original one. For the purpose of demonstration, we binned these results based on number of spikes used into bins of width 10. The percentage of rank-2 solutions is shown in Figure 9A as a function of number of measurements. The mean SNR is shown in Figure 9B.

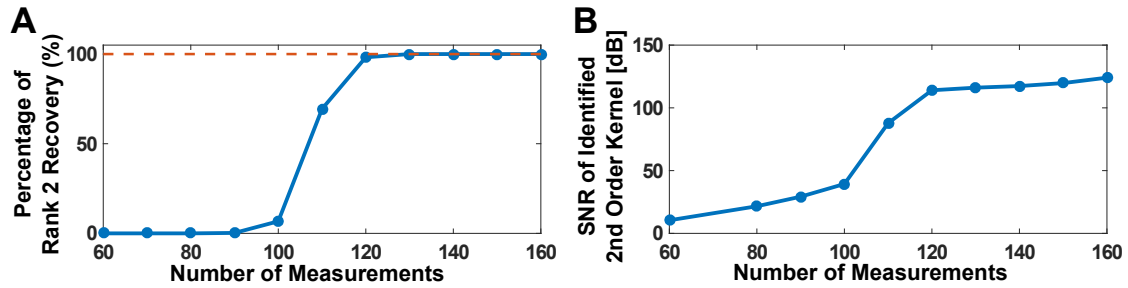


Figure 9: Example of low-rank functional identification. (A) Percentage of successful rank-2 recovery in identification. (B) Mean SNR of identified second order DSP kernel.

It can be seen from Figure 9B that the identification algorithm presented here is able to recover the underlying DSP with exceptional accuracy using a reasonable and tractable number of measurements.

3.3 Evaluation of Functional Identification of a Neural Circuit of Complex Cells by Decoding

In Section 3.1, we have shown that the sparse decoding algorithm requires much less number of neurons and measurements (spikes) in the reconstruction of stimuli encoded by a neural circuit of complex cells. We have also demonstrated in Section 3.2 that the proposed sparse functional identification algorithm enables the identification of complex cells with a tractable number of measurements. Together, the two algorithms afford us tractable functional identification of an entire neural circuit of complex cells that is capable of fully representing stimuli information, in that i) the size of the neural circuit is tractable, and ii) the requirement for functional identification is tractable.

Decoding of visual stimuli by identified linear filters has previously been considered in [41]. In [17], it was shown that the evaluation of functional identification of an entire neural circuit can be more intuitively performed in the input space by decoding the stimuli with identified circuit parameters. Here, we extend the previous results and apply such evaluation procedure

on the sparse decoding and sparse functional identification algorithms. The procedure is described as follows. First, each complex cell is functionally identified using Algorithm 5 or Algorithm 6. Second, novel stimuli are presented to the neural circuit. Third, the spike trains observed are used to reconstruct the encoded novel stimuli by the sparse decoding algorithm, assuming that the circuit parameters take the identified values. Finally, SNR of the reconstruction can be obtained. A high SNR indicates a well identified circuit while a low number implies that the functional identification of the neural circuit is not of good quality. The latter can be caused by a lack of number of measurements used in functional identification, or by a lack of complex cells in the neural circuit.

We performed the functional identification of all 19 complex cells in the neural circuit given in the example in Section 3.1.3. We first identified all complex cells by presenting to the neural circuit M temporal stimuli. We repeated the identification of the entire circuit using 8 different values of M . We then presented to the same circuit (with the original DSPs as in Section 3.1.3), 100 novel stimuli drawn from the input space and used the spike times generated by the neural circuit to decode the stimuli. In the decoding process however, we assumed that the DSPs of the set of complex cells are as identified, for all 8 values of M . The mean reconstruction SNR of the 100 stimuli is shown in Figure 10. As shown, the quality of reconstruction is low until enough trials were used in identification. When more than 19 trials were performed, perfect reconstruction of the entire neural circuit was achieved. The dimension of the stimulus space was 41 and the average number of spikes per neuron used for identification varied from 44 for 6 trials to 202 for 28 trials.

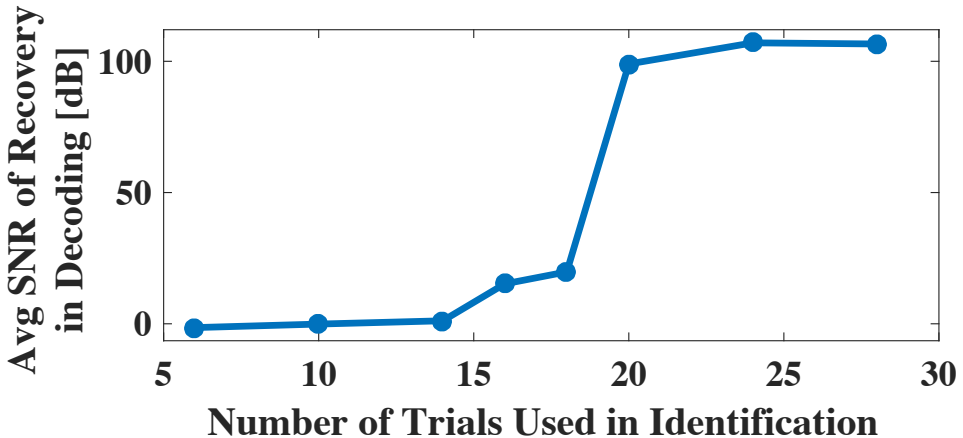


Figure 10: Evaluating identification quality in the input space by plotting the average SNR of reconstruction of novel stimuli assumed to be encoded with the identified DSPs.

4 Low-Rank Decoding and Functional Identification of Complex Cells with Spatio-Temporal Stimuli

The framework introduced in Section 3 can be extended to the sparse decoding of spatio-temporal stimuli and the sparse identification of spatio-temporal DSPs of complex cells.

Details of the extension to the spatio-temporal case are provided in Appendix B-D. In what follows, we present spatio-temporal examples of sparse decoding and identification.

4.1 Low-Rank Decoding of Spatio-Temporal Visual Stimuli

The stimuli u_1 considered here have p spatial dimensions and a single temporal dimension, *i.e.*, $u_1 = u_1(x_1, x_2, \dots, x_p, t)$. For simplicity of notation, we use a compact, vector notation and denote the spatial variables as $\mathbf{x} = (x_1, x_2, \dots, x_p)$. When $p = 2$, u_1 is the usual 2-D visual stimulus. The definition of the space of input stimuli is provided in Appendix B.

The encoding of spatiotemporal stimuli by a population of complex cells, and the sparse decoding of spatiotemporal stimuli are formally described in Appendix C. Note that the output of the DSP of each neuron $i = 1, 2, \dots, M$, can be expressed as

$$v^i(t) = \int_{\mathbb{D}^2} h_2^i(\mathbf{x}_1, t - s_1; \mathbf{x}_2, t - s_2) u_1(\mathbf{x}_1, s_1) u_1(\mathbf{x}_2, s_2) d\mathbf{x}_1 d\mathbf{x}_2 ds_1 ds_2, \quad (64)$$

Here

$$h_2^i(\mathbf{x}_1, t_1; \mathbf{x}_2, t_2) = g_1^{i1}(\mathbf{x}_1, t_1) g_1^{i1}(\mathbf{x}_2, t_2) + g_1^{i2}(\mathbf{x}_1, t_1) g_1^{i2}(\mathbf{x}_2, t_2) \quad (65)$$

has low-rank [18].

In this section we provide examples that demonstrate the tractability of sparse decoding of spatio-temporal stimuli encoded with complex cells using a small number of spikes.

4.1.1 Example - Decoding of 2D Spatio-Temporal Stimuli

We first present an example in which \mathbf{x} is one-dimensional, *i.e.*, $\mathbf{x} = x_1$. In this example, our main focus is to illustrate how the number of spikes affects the reconstruction of stimuli encoded by complex cells.

The neural circuit we consider here consists of 62 direction selective complex cells. The low-rank DSPs of the complex cells are of the form

$$h_2^i(\mathbf{x}_1, t_1; \mathbf{x}_2, t_2) = g_1^{i1}(\mathbf{x}_1, t_1) g_1^{i1}(\mathbf{x}_2, t_2) + g_1^{i2}(\mathbf{x}_1, t_1) g_1^{i2}(\mathbf{x}_2, t_2), \quad (66)$$

where $g_1^{i1}(\mathbf{x}, t)$ and $g_1^{i2}(\mathbf{x}, t)$ are quadrature pairs of spatio-temporal Gabor filters and $i = 1, \dots, M$. The Gabor filters are constructed from dilations and translations of the mother wavelets on a dyadic grid, where the mother functions can be expressed as

$$g_1^1(\mathbf{x}, t) = \exp \left(- \left(\frac{x_1^2}{8} + \frac{t^2}{0.001} \right) \right) \cos(1.5x_1 + 20\pi t) \quad (67)$$

and

$$g_1^2(\mathbf{x}, t) = \exp \left(- \left(\frac{x_1^2}{8} + \frac{t^2}{0.001} \right) \right) \sin(1.5x_1 + 20\pi t). \quad (68)$$

The BSG of the complex cells are IAF neurons with bias $b^i = 10$ and integration constant $\kappa = 1$, for $i = 1, \dots, M$. These two parameters are kept the same for all stimuli. Different

threshold values are chosen for the IAF neurons in order to vary the total number of spikes in a larger range to evaluate how many measurements are required for a perfect reconstruction of input stimuli.

The domain of the input space \mathcal{H}_1^1 is $\mathbb{D} = [0, 32] \times [0, 0.4]$ ([a.u.] and [sec], respectively) and $L_{x_1} = 6, L_t = 4, \Omega_{x_1} = 0.1875 \cdot 2\pi, \Omega_t = 10 \cdot 2\pi$ [rad/sec]. Thus, $\dim(\mathcal{H}_1^1) = 117$. Stimuli were randomly generated by choosing the basis coefficients to be i.i.d. Gaussian random variables.

We tested the encoding of 1,416 stimuli. Each time, a different number of spikes was generated. The reconstruction of stimuli was performed in MATLAB using the extended Algorithm 3, and the SDPs were solved using SDPT3 [34].

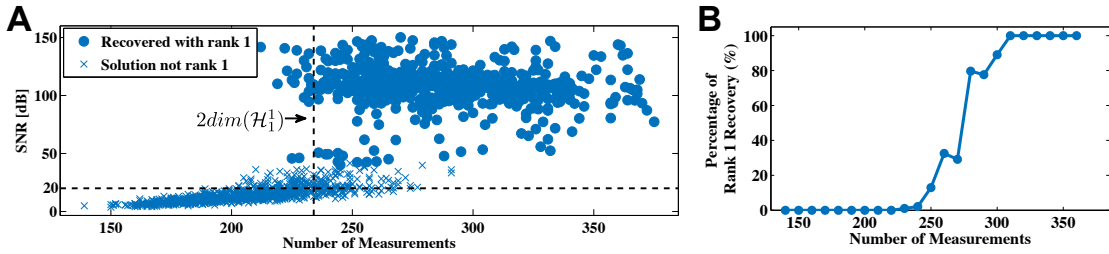


Figure 11: Example of low-rank decoding of spatio-temporal stimuli. (A) Effect of number of measurements (spikes) on reconstruction quality. (B) Percentage of exact rank 1 solutions.

The SNR of all reconstructions is depicted in the scatter plot of Figure 11A. Here solid dots represent exact rank 1 solutions (largest eigenvalue is at least 100 times larger than the sum of the rest of the eigenvalues), and crosses indicate that the trace minimization found a higher rank solution with a smaller trace. The percentage of exact rank 1 solutions is shown in Figure 11B. Similar to phase transition phenomena in other sparse recovery algorithms [35], a relatively sharp transition (around 50 spikes) from very low probability of recovery to very high probability of perfect reconstruction can be seen. It can also be seen that the number of measurements that are needed for perfect recovery is substantially lower than the 6,965 spikes required by Algorithm 1.

4.1.2 Example - Decoding of 3D Spatio-Temporal Stimuli

Next, we present two examples of decoding of spatio-temporal visual stimuli encoded by a population of complex cells. Here, $\mathbf{x} = (x_1, x_2)$ and the Volterra DSPs of the complex cells are of the form

$$h_2^i(\mathbf{x}_1, t_1; \mathbf{x}_2, t_2) = g_1^{i1}(\mathbf{x}_1, t_1)g_1^{i2}(\mathbf{x}_2, t_2) + g_1^{i2}(\mathbf{x}_1, t_1)g_1^{i1}(\mathbf{x}_2, t_2), \quad (69)$$

where $g_1^{i1}(\mathbf{x}, t)$ and $g_1^{i2}(\mathbf{x}, t)$ are, for simplicity, quadrature pairs of spatial-only Gabor filters and $i = 1, \dots, M$. The Gabor filters are constructed using a dyadic grid of dilations, translations and rotations of the following pair of mother wavelets [15],

$$g_1^1(\mathbf{x}, t) = \exp\left(-\frac{1}{8}(4x_1^2 + 2x_2^2)\right) \cos(2.5x_1) \quad (70)$$

and

$$g_1^2(\mathbf{x}, t) = \exp\left(-\frac{1}{8}(4x_1^2 + 2x_2^2)\right) \sin(2.5x_1). \quad (71)$$

The ensemble of Gabor filters forms a frame in the spatial domain of the input space [42].

For the first example, a 0.4-second-long synthetically generated video sequence is encoded by the neural circuit. The order of the input space was chosen to be $L_{x_1} = L_{x_2} = 3, L_t = 4$. Thus, the dimension of the input space is 441. The input stimulus was created by choosing its basis coefficients to be i.i.d. Gaussian random variables. The stimulus was encoded by a neural circuit consists of 318 complex cells. A total of 1,374 spikes were generated by the encoding circuit. The stimulus was decoded using the extended Algorithm 3. As shown in Figure 12, the video sequence can be perfectly reconstructed with a fairly small number of spikes (A snapshot of the video is shown, see also Supplementary Video S1 for full video). The SNR of the reconstructed video was 92.8 [dB], thereby reaching almost perfect reconstruction with machine precision. Note that without the reconstruction algorithm employed here, 97,461 measurements would be required from at least 5,733 complex cells to achieve perfect reconstruction.

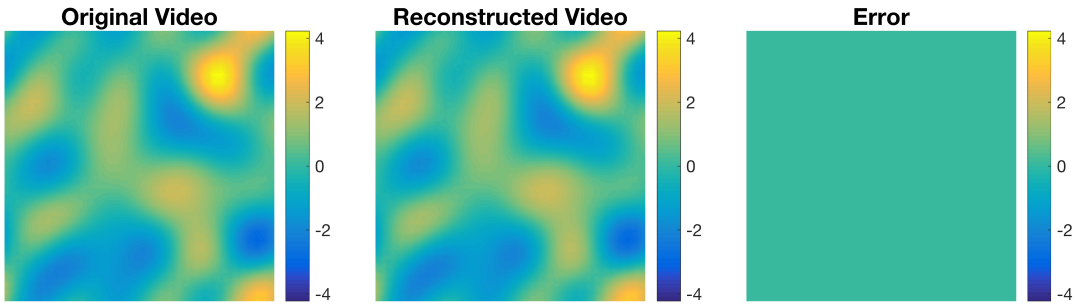


Figure 12: Example of reconstruction of synthesized visual stimuli. A synthetically generated visual stimulus was encoded by 318 Complex Cells that generated some 1,374 spikes. A snapshot of the original video is shown on the left. The reconstruction is shown in middle and the error on the right. SNR 92.8 [dB]. (See also Supplementary Video S1)

We then performed encoding and subsequent reconstructions of 2-second long natural video sequences that had a resolution of 72×128 pixels. The videos had temporal bandwidth of 10[Hz] and spatial bandwidth of 0.375 cycles per pixel. Additionally, the spatial bandwidth was restricted to a circular area to make it isotropically bandlimited. The videos were encoded by a neural circuit consisting of 21,776 complex cells, whose DSPs were modeled as spatial-only quadrature pair of Gabor filters. The Gabor filters formed a frame in the spatial dimension of the space.

The decoding was performed using 6 NVIDIA P100 GPUs on a single computer node. Despite of their computational power, the amount of memory required by the algorithm for decoding the whole video sequence exceeded the memory capacity of the 6 GPUs. Therefore, the reconstruction of the entire video was performed by decoding 0.2 second long segments of the video independently and then stitching them together [16]. The overlap between consecutive segments was 0.1 second. We chose the order of the space to be $L_{x_1} = 27, L_{x_2} = 48, L_t = 3$,

and the bandwidth of the space to be $\Omega_{x_1} = \Omega_{x_2} = 0.75\pi[\text{rads/pixel}]$ and $\Omega_t = 20\pi[\text{rads/s}]$. We also restricted the spectral lines in the spatial dimension to be inside a circular area instead of a square area as defined in (73), *i.e.*, we considered only l_{x_1} and l_{x_2} that are in the set $\{(l_{x_1}, l_{x_2}) | l_{x_1}^2 L_{x_2}^2 + l_{x_2}^2 L_{x_1}^2 \leq L_{x_1}^2 L_{x_2}^2\}$. This allowed the bandwidth of the stimuli to be covered with minimal number of spectral lines [16]. Note that, by the construction of input space, the decoded video must be periodic in time. However, an arbitrary 0.2-second video may not be periodic. Therefore, we chose the decoding space to have a temporal period of 0.3 seconds and retained only the middle 0.2 seconds of the reconstructed segments. The total dimension of the decoding space was 28,413. The extended Algorithm 4 was used in decoding.

For the example depicted in Figure 13A, a total of 980,730 spikes were generated by the neural circuit. About 76,000 to 86,500 measurements were used in reconstructing the video in each time segment. This is approximately 2.67 to 3.04 times of the dimension of the space. In contrast, a total of 403,663,491 measurements would have been required by Algorithm 1 to reconstruct the same video. In Figure 13A, a snapshot of the original, reconstructed video sequence and the error are shown (see also Supplementary Video S2) The SNR of the reconstructed video was 48.85 [dB] (the first and last 20 milliseconds were removed from the SNR calculation due to boundary conditions).

Additional examples of reconstructed natural video encoded by the same neural circuit are shown in Figure 13B-E (see also Supplementary Video S3-S6).

4.2 Low-Rank Functional Identification of Spatio-Temporal Complex Cells

The low-rank functional identification described in Section 3.2 can be extended to identify DSPs of spatio-temporal complex cells. The functional identification for the spatio-temporal case is formally described in Appendix D.

In this section we first provide an example of identification of spatio-temporal DSPs of complex cells. We then evaluate the identified low-rank spatio-temporal DSPs by decoding novel stimuli encoded with the original neural circuit. The decoding uses the identified filters. Finally, we compare the performance of the low-rank identification methodology with other identification algorithms.

4.2.1 Example - Low-Rank Functional Identification of Complex Cell DSP from Spike Times in Response to Spatio-Temporal Stimuli

In this example, we first consider identifying the DSP of a single complex cell in the neural circuit used in Section 4.1.1. As a reminder, the neural circuit used in the example in Section 4.1.1 encodes spatio-temporal stimuli of the form $u_1(x_1, t)$.

We presented to the population of M complex cells 0.4-second stimuli, where M varied from 40 to 80. The stimuli were generated by choosing their basis coefficients as i.i.d. Gaussian random variables. For each M , we repeated the functional identification process

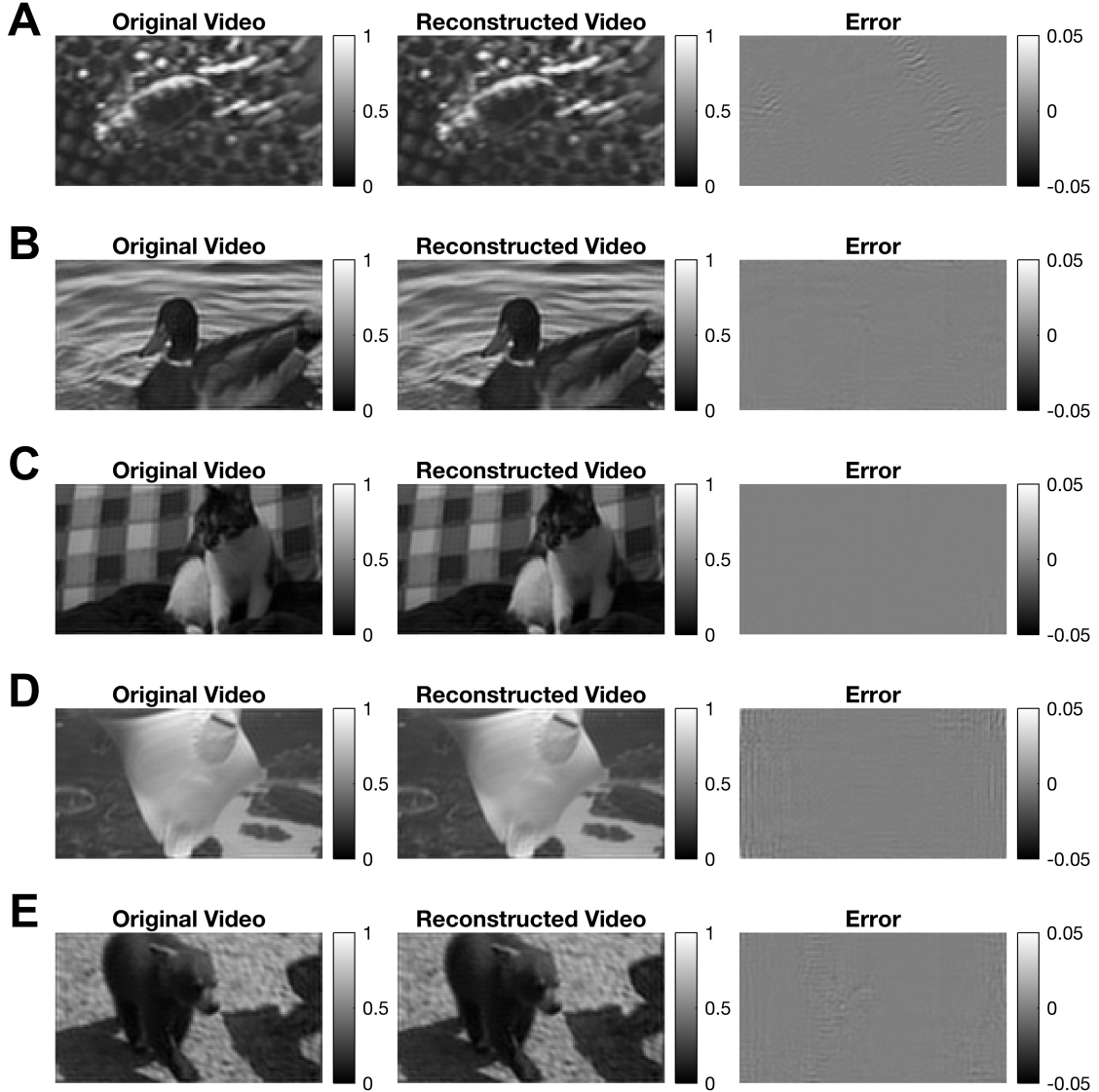


Figure 13: Examples of reconstruction of natural visual stimuli. Snapshots of the original videos encoded by a neural circuit with complex cells are shown on the left. The reconstructions from the spike times are shown in the middle and the error on the right. Note that the color bar indicating the magnitude of the error was set to 10% of the input range. SNR: (A) 48.85 [dB]. (B) 46.92 [dB]. (C) 48.61 [dB]. (D) 50.76 [dB]. (E) 48.11 [dB]. (See also Supplementary Videos S2-S6)

for 200 times, each with different stimuli. Identification was essentially based on the extended Algorithm 3, where the SDPs were again solved by SDPT3.

The percentage of rank 2 solutions is shown in Figure 14A as a function of number of experimental trials. The mean SNR is shown in Figure 14B. Figure 14A suggests that, if the number of trials is larger than 70, the solution to the trace minimization coincides with high probability with the rank minimization problem. In contrast, identification of the complex cell DSP using Algorithm 2 would have required at least 407 trials.

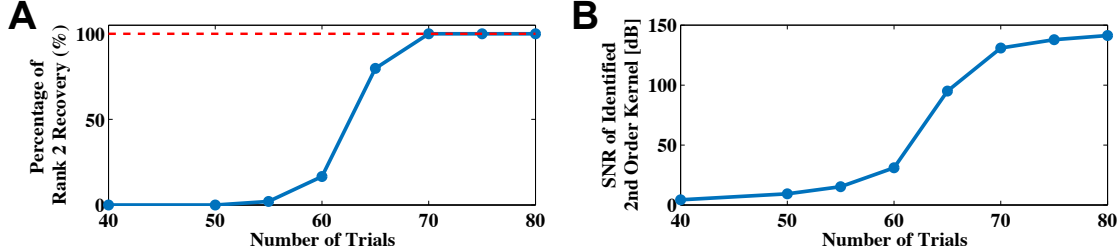


Figure 14: Example of low-rank functional identification of spatio-temporal complex cells. (A) Percentage of successful rank 2 recovery in identification. (B) Mean SNR of identified second order DSP kernel.

It can be easily seen that the identification process does not require a large number of trials to achieve perfect identification, thereby enabling the identification of non-linear dendritic processing of cells similar in structure to complex cells with a tractable amount of physiological recordings.

4.2.2 Example - Evaluation of Functional Identification of Neural Circuit of Complex Cells Using Decoding

We then performed the functional identification of all 62 complex cells in the neural circuit used of the example in Section 4.1.1. Here, our goal is to evaluate the identification quality using decoding.

We first identified all complex cells by presenting to the neural circuit M spatio-temporal stimuli. We also performed the identification of the entire circuit using 8 different values of M . We then presented to the same circuit 100 novel stimuli drawn from the input space and used the spike times generated by the neural circuit to decode the stimuli. In the decoding process, we assumed that the DSPs of the set of complex cells are as identified, for all 8 values of M . The mean reconstruction SNR of the 100 stimuli is shown in Figure 15. As shown, the quality of reconstruction was kept at low SNR until enough trials were used in identification. When more than 70 trials were performed, perfect reconstruction was achieved, and thereby the entire neural circuit has been identified with a very high quality.

4.2.3 Comparison with STC, GQM and NIM

We compared the performance of the low-rank functional identification algorithm introduced here with the widely used Spike-Triggered Covariance (STC) algorithm [38]. As in

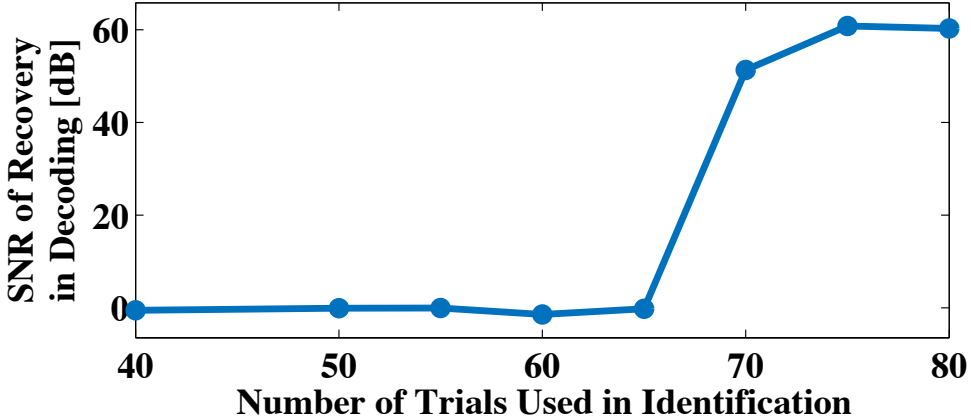


Figure 15: Evaluating identification quality in the input space. SNR of reconstruction of novel stimuli assumed to be encoded with the identified DSPs.

Section 4.2.1, a complex cell with a pair of orthogonal Gabor filters was chosen for identification. However, the filters had different norms.

Figure 16A shows the quality of identification (SNR) as the number of spikes used in identification increases. Note that the low-rank functional identification algorithm reached perfect identification using only 746 spikes, whereas the performance of the STC algorithm saturated at ~ 17 [dB] after almost 40,000 spikes were used. Figure 16B shows the identified individual Gabor filters of the complex cells using both algorithms. The number of spikes used are indicated at the top of each column.

We also evaluated the identification performance of the generalized quadratic model (GQM) [44] and the non-linear input model (NIM) [45] with quadratic upstream filters to the same example above. The results (not shown) were similar to those obtained with the STC algorithm.

We note that while the low-rank functional identification algorithm is formulated as non-linear sampling using TEMs and solved using recent advances in low-rank matrix sensing, the other algorithms tested here rely on moment based or likelihood based methods that require a large number of samples to converge.

5 Conclusions

In this paper, we presented sparse algorithms for the reconstruction of temporal as well as spatio-temporal stimuli from spike times generated by neural circuits consisting of complex cells. We formulated the encoding as generalized sampling in a tensor space and exploited the low-rank structure of the stimulus in this space, leading to tractable reconstruction algorithms. For neural circuits consisting of complex cells, this suggests that, in addition to each complex cell extracting visual features, a biologically plausible number of complex cells are capable of faithfully representing visual stimuli. In particular, the examples with natural video sequences provided in this paper, demonstrate that neural circuits with non-linear

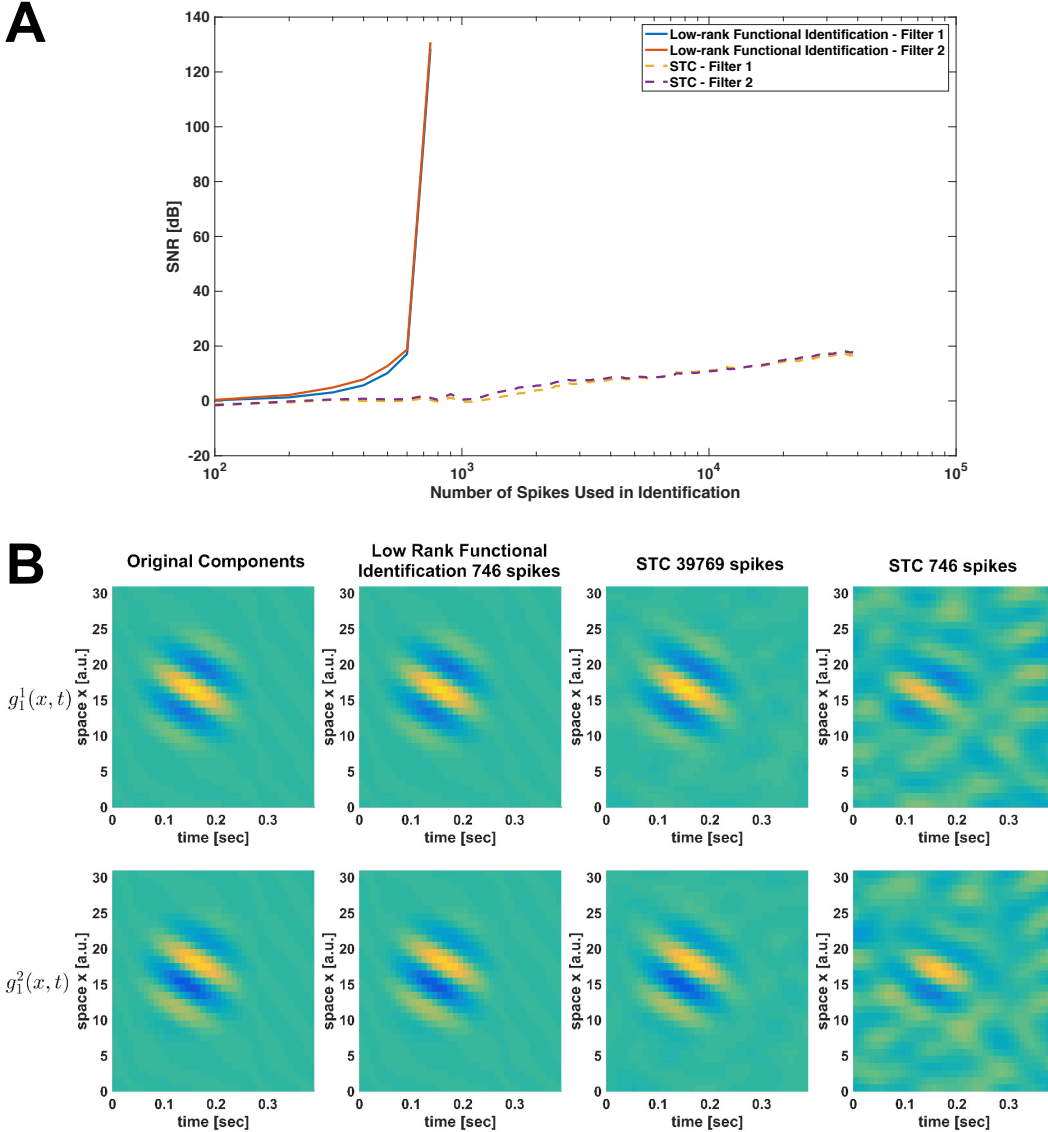


Figure 16: Comparison of the low-rank functional identification with STC. (A) SNR of identified quadrature pairs of Gabor filters in a complex cell, as a function of number of spikes used in identification. Low-rank functional identification reaches nearly machine precision with about 746 spikes, which corresponds to about 70 stimulus trials (see also Figure 14). STC reaches about 17 [dB] SNR with $\sim 30,000$ spikes. (B) Quadrature pair Gabor filters (1st column) identified with low-rank functional identification algorithm with 746 spikes (2nd column, SNR: 128.48 [dB], 130.84 [dB]), and with STC using 39,769 spikes (3rd column, SNR: 16.79 [dB], 17.88 [dB]) and using 746 spikes (4th column, SNR: 0.20 [dB], 0.60 [dB]).

receptive fields and highly non-linear spike generating mechanisms, are able to faithfully represent natural visual stimuli. The number of spikes that increases just quasi-linearly with the bandwidth or resolution of the stimuli.

Based on duality between sparse decoding and functional identification, we showed that functional identification of complex cells DSPs can be efficiently achieved by exploiting their low-rank structure, using similar algorithms as used in decoding. These algorithms make the functional identification of complex cells tractable, allowing guaranteed high quality identification using a much smaller set of testing stimuli as well as of shorter time duration.

The mathematical treatment presented here, however, is not limited to the complex cells in V1. It can be applied to other neural circuits of interest. For example, early olfactory coding in fruit flies [46] and auditory encoding in grasshoppers [47] have also been shown to have the structure of low-rank DSP kernels. Moreover, the Hassenstein-Reichardt detector [48], a popular model for elementary motion detectors in fruit flies, is also I/O equivalent to low-rank DSP kernels.

Competing Interests

The authors declare that they have no competing interests.

Acknowledgments

The research reported here was supported by AFOSR under grant #FA9550-16-1-0410.

References

- [1] David H. Hubel and Torsten N. Wiesel. Receptive field, binocular interaction and functional architecture in the cat's visual cortex. *Journal of Physiology*, 160(1):106–154, 1962.
- [2] H. B. Barlow and W. R. Levick. The mechanism of directionally selective units in rabbit's retina. *The Journal of Physiology*, 178(3):477, 1965.
- [3] Clay R. Reid and Jose-Manuel Alonso. Specificity of monosynaptic connections from thalamus to visual cortex. *Nature*, 378(6554):281–284, 11 1995.
- [4] Jose-Manuel Alonso and Luis M. Martinez. Functional connectivity between simple cells and complex cells in cat striate cortex. *Nature Neuroscience*, 1:Functional connectivity between simple cells and complex cells in cat striate cortex, 1998.
- [5] Daniel A. Pollen and Steven F. Ronner. Spatial computation performed by simple and complex cells in the visual cortex of the cat. *Vision Research*, 22(1):101 – 118, 1982.
- [6] D. L. Ringach and M. J. Hawken. Orientation selectivity in macaque v1: diversity and laminar dependence. *Journal of Neuroscience*, 22:5639–5651, 2002.
- [7] Peter Dayan and L.F. Abbott. *Theoretical Neuroscience: Computational and Mathematical Modeling of Neural Systems*. MIT Press, Cambridge, MA, 2001.
- [8] Nicole C. Rust, Odelia Schwartz, J. Anthony Movshon, and Eero P. Simoncelli. Spatiotemporal elements of macaque v1 receptive fields. *Neuron*, 46:945–956, 2005.
- [9] Edward H. Adelson and James R. Bergen. Spatiotemporal energy models for the perception of motion. *Journal of Optical Society of America. A, Optics and Image Science*, 2(2):284–299, 1985.
- [10] Jon Tournyan, Gidon Felsen, and Yang Dan. Spatial structure of complex cell receptive fields measured with natural images. *Neuron*, 45:781–791, 2005.
- [11] Matteo Carandini, Jonathan B. Demb, Valerio Mante, David J. Tolhurst, Yang Dan, Bruno A. Olshausen, Jack L. Gallant, and Nicole C. Rust. Do we know what the early visual system does? *Journal of Neuroscience*, 24(46):10577–10597, 2005.
- [12] Rodney Douglas, Henry Markram, and Kevan Martin. *The Synaptic Organization of the Brain*, chapter Neocortex. Oxford University Press, 5th ed. edition, 2004.
- [13] P. Hammond. Directional tuning of complex cells in area 17 of the feline visual cortex. *The Journal of Physiology*, 285(1):479–491, 1978.
- [14] Russell L. De Valois, Duane G. Albrecht, and Lisa G. Thorell. Spatial frequency selectivity of cells in macaque visual cortex. *Vision Research*, 22(5):545 – 559, 1982.
- [15] Aurel A. Lazar, Eftychios A. Pnevmatikakis, and Yiyin Zhou. Encoding natural scenes with neural circuits with random thresholds. *Vision Research*, 50(22):2200–2212, October 2010. Special Issue on Mathematical Models of Visual Coding.

- [16] Aurel A Lazar and Yiyin Zhou. Reconstructing natural visual scenes from spike times. *Proceedings of the IEEE*, 102(10):1500–1519, 2014.
- [17] Aurel A Lazar and Yiyin Zhou. Identifying multisensory dendritic stimulus processors. *IEEE Transactions on Molecular, Biological and Multi-Scale Communications*, 2(2):183–198, 2016.
- [18] Aurel A. Lazar and Yevgeniy B. Slutskiy. Spiking Neural Circuits with Dendritic Stimulus Processors. *Journal of Computational Neuroscience*, 38(1):1–24, 2015.
- [19] Aurel A. Lazar and Yiyin Zhou. Volterra Dendritic Stimulus Processors and Biophysical Spike Generators with Intrinsic Noise Sources. *Frontiers in Computational Neuroscience*, 8, 2014.
- [20] Vasilis Z. Marmarelis. *Nonlinear Dynamic Modeling of Physiological Systems*. Wiley-IEEE Press, 2004.
- [21] Emmanuel J. Candès, Yonina C. Eldar, Thomas Strohmer, and Vladislav Voroninski. PhaseLift: Exact and stable signal recovery from magnitude measurements via convex programming. *Communications in Pure and Applied Mathematics*, 66(8):1241–1274, 2011.
- [22] Emmanuel J. Candès and Benjamin Recht. Exact matrix completion via convex optimization. *Foundations of Computational Mathematics*, 2009(9):717–772, 2009.
- [23] Benjamin Recht, Maryam Fazel, and Pablo A. Parrilo. Guaranteed minimum-rank solutions of linear matrix equations via nuclear norm minimization. *SIAM Review*, 52(3):471–501, 2010.
- [24] Wilson J. Rugh. *Nonlinear System Theory: Volterra/Wiener Approach*. Johns Hopkins University Press, Baltimore, MD, 1981.
- [25] A.L. Hodgkin and A.F. Huxley. A quantitative description of membrane current and its application to conduction and excitation in nerve. *Journal of Physiology*, 117(4):500–44, 1952.
- [26] C. Morris and H. Lecar. Voltage oscillations in the barnacle giant muscle fiber. *Biophysical Journal*, 35(1):193–213, Jul 1981.
- [27] Eugene M Izhikevich. Simple model of spike neurons. *IEEE Transactions on Neural Networks*, 14(6):1569–1572, 2003.
- [28] Aurel A. Lazar. Population encoding with hodgkin-huxley neurons. *IEEE Transactions on Information Theory*, 56(2):821–837, February 2010. Special Issue on Molecular Biology and Neuroscience.
- [29] Justin Keat, Pamela Reinagel, R. Clay Reid, and Markus Meister. Predicting every spike: A model for the responses of visual neurons. *Neuron*, 30:803–817, 2001.
- [30] Andrzej Cichocki, Rafal Zdunek, Anh Huy Phan, and Shun-ichi Amari. *Nonnegative Matrix and Tensor Factorizations: Applications to Exploratory Multi-way Data Analysis and Blind Source Separation*. Wiley, October 2009.

- [31] M. Fazel, H. Hindi, and S. Boyd. Rank minimization and applications in system theory. In *Proceedings American Control Conference*, pages 3273–3278, June 2004.
- [32] Emmanuel J. Candès, Yonina C. Eldar, Thomas Strohmer, and Vladislav Voroninski. Phase retrieval via matrix completion. *SIAM Journal of Imaging Science*, 6(1):199–225, 2013.
- [33] Prateek Jain, Praneeth Netrapalli, and Sujay Sanghavi. Low-rank matrix completion using alternating minimization. In *Proceedings of the Forty-fifth Annual ACM Symposium on Theory of Computing*, STOC ’13, pages 665–674, New York, NY, USA, 2013. ACM.
- [34] R. H. Tutuncu, K. C. Toh, and M. J. Todd. Solving semidefinite-quadratic-linear programs using sdpt3. *Mathematical Programming Ser. B*, 95:189–217, 2003.
- [35] David L. Donoho, Arian Maleki, and Andrea Montanari. Message-passing algorithms for compressed sensing. *PNAS*, 106(45):18914–18919, 2009.
- [36] Liam Paninski. Convergence properties of some spike-triggered analysis techniques. In *Advances in neural information processing systems*, pages 189–196, 2003.
- [37] Odelia Schwartz, EJ Chichilnisky, and Eero P Simoncelli. Characterizing neural gain control using spike-triggered covariance. In *Advances in neural information processing systems*, pages 269–276, 2002.
- [38] Jonathan W. Pillow and Eero P. Simoncelli. Dimensionality reduction in neural models: an information-theoretic generalization of spike-triggered average and covariance analysis. *Journal of Vision*, 6(4):414–428, 2006.
- [39] Odelia Schwartz, Jonathan W. Pillow, Nicole C. Rust, and Eero P. Simoncelli. Spike-triggered neural characterization. *Journal of Vision*, 6:484–207, 2006.
- [40] Il Memming Park and Jonathan W Pillow. Bayesian spike-triggered covariance analysis. In *Advances in neural information processing systems*, pages 1692–1700, 2011.
- [41] Garrett Stanley, Fei F. Li, and Yang Dan. Reconstruction of natural scenes from ensemble responses in the lateral geniculate nucleus. *Journal of Neuroscience*, 19(18):8036–8042, 1999.
- [42] Tai Sing Lee. Image representation using 2d gabor wavelets. *IEEE Transactions on Pattern Analysis and Machine Intelligence*, 18(10):1–13, 1996.
- [43] Ladan Shams and Christoph von der Malsburg. The role of complex cells in object recognition. *Vision Research*, 42:2547–2554, 2002.
- [44] Il M Park, Evan W Archer, Nicholas Priebe, and Jonathan W Pillow. Spectral methods for neural characterization using generalized quadratic models. In *Advances in neural information processing systems*, pages 2454–2462, 2013.
- [45] James M McFarland, Yuwei Cui, and Daniel A Butts. Inferring nonlinear neuronal computation based on physiologically plausible inputs. *PLoS Comput Biol*, 9(7):e1003143, 2013.

- [46] A. J. Kim, A. A. Lazar, and Y. B. Slutskiy. System identification of drosophila olfactory sensory neurons. *Journal of Computational Neuroscience*, 30(1):143–161, Feb 2011.
- [47] Jan Clemens, Sandra Wohlgemuth, and Bernhard Ronacher. Nonlinear computations underlying temporal and population sparseness in the auditory system of the grasshopper. *Journal of Neuroscience*, 32(29):10053–10062, 2012.
- [48] Bernhard Hassenstein and Werner Reichardt. Systemtheoretische analyse der zeit-, reihenfolgen- und vorzeichenauswertung bei der bewegungsperzeption des rüsselkäfers chlorophanus,. *Z. Naturforsch. B*, 11(9):513–524, 1956.

A Proof of Lemma 2

Proof: With (18) the t-transform for the i^{th} stimulus is given by

$$\int_{t_k^i}^{t_{k+1}^i} \int_{\mathbb{D}^2} h_2(t - s_1; t - s_2) u_2^i(s_1; s_2) ds_1 ds_2 dt = q_k^i.$$

Since $\mathcal{P}_2 u_2^i = u_2^i$, we have

$$\begin{aligned} & \int_{t_k^i}^{t_{k+1}^i} \int_{\mathbb{D}^2} h_2(t - s_1; t - s_2) (\mathcal{P}_2 u_2^i)(s_1; s_2) ds_1 ds_2 dt = q_k^i \quad \text{or} \\ & \int_{t_k^i}^{t_{k+1}^i} \int_{\mathbb{D}^2} \int_{\mathbb{D}^2} h_2(t - s_1; t - s_2) K_2(s_1, s_2; s'_1, s'_2) u_2^i(s'_1; s'_2) ds'_1 ds'_2 ds_1 ds_2 dt = q_k^i \quad \text{or} \\ & \int_{t_k^i}^{t_{k+1}^i} \int_{\mathbb{D}^2} \int_{\mathbb{D}^2} h_2(t - s_1; t - s_2) K_2(t - s_1, t - s_2; t - s'_1, t - s'_2) ds_1 ds_2 u_2^i(s'_1; s'_2) ds'_1 ds'_2 dt = q_k^i \quad \text{or} \\ & \int_{t_k^i}^{t_{k+1}^i} \int_{\mathbb{D}^2} (\mathcal{P}_2 h_2)(t - s_1; t - s_2) u_2^i(s_1; s_2) ds_1 ds_2 dt = q_k^i. \end{aligned}$$

Finally, with (17), we obtain

$$\mathcal{L}_k^i(\mathcal{P}_2 h_2) = q_k^i, k \in \mathbb{I}^i, i = 1, \dots, M. \quad (72)$$

□

B Modeling of Spatio-Temporal Stimuli

Definition 4. The space of trigonometric polynomials \mathcal{H}_1^p is the Hilbert space of complex-valued functions

$$u_1(\mathbf{x}, t) = \sum_{\mathbf{l}_x} \sum_{l_t} c_{\mathbf{l}_x l_t} e_{\mathbf{l}_x l_t}(\mathbf{x}, t), \quad (73)$$

where

$$\mathbf{l}_{\mathbf{x}} \in \{(l_{x_1}, l_{x_2}, \dots, l_{x_p}) \in \mathbb{Z}^p \mid -L_{x_1} \leq l_{x_1} \leq L_{x_1}, -L_{x_2} \leq l_{x_2} \leq L_{x_2}, \dots, -L_{x_p} \leq l_{x_p} \leq L_{x_p}\},$$

$$l_t \in \{k \in \mathbb{Z} \mid -L_t \leq k \leq L_t\}$$

over the domain \mathbb{D} , where, by abuse of notation, $\mathbb{D} = [0, S_{x_1}] \times [0, S_{x_2}] \times \dots \times [0, S_{x_p}] \times [0, S_t]$ and $S_t = \frac{2\pi L_t}{\Omega_t}$, $S_{x_1} = \frac{2\pi L_{x_1}}{\Omega_{x_1}}$, $S_{x_2} = \frac{2\pi L_{x_2}}{\Omega_{x_2}}$, \dots , $S_{x_p} = \frac{2\pi L_{x_p}}{\Omega_{x_p}}$. In addition, $e_{\mathbf{l}_{\mathbf{x}} l_t}(\mathbf{x}, t) = e_{\mathbf{l}_{\mathbf{x}}}(\mathbf{x}) e_{l_t}(t)$ where

$$e_{\mathbf{l}_{\mathbf{x}}}(\mathbf{x}) = \frac{1}{\sqrt{\prod_{i=1}^p S_i}} \exp\left(j \omega_{\mathbf{x}}^T \mathbf{x}\right) \quad ; \quad \omega_{\mathbf{x}} = \left(\frac{l_{x_1} \Omega_{x_1}}{L_{x_1}}, \frac{l_{x_2} \Omega_{x_2}}{L_{x_2}}, \dots, \frac{l_{x_p} \Omega_{x_p}}{L_{x_p}}\right)$$

and

$$e_{l_t}(t) = \frac{1}{\sqrt{S_t}} \exp\left(\frac{j l_t \Omega_t}{L_t} t\right).$$

Here Ω_t denotes the bandwidth, and L_t the order of the space in the temporal domain while Ω_{x_i} and L_{x_i} denote the bandwidth and order of the space in the i^{th} spatial variable. Stimuli $u_1 \in \mathcal{H}_1^p$ are periodic with periods $S_t, S_{x_1}, \dots, S_{x_p}$.

We denote the temporal dimension of \mathcal{H}_1^p by $\dim_t(\mathcal{H}_1^p) = 2L_t + 1$ and the total dimension by $\dim(\mathcal{H}_1^p) = (2L_t + 1) \prod_{i=1}^p (2L_{x_i} + 1)$.

Definition 5. The tensor product space $\mathcal{H}_2^p = \mathcal{H}_1^p \otimes \mathcal{H}_1^p$ is a Hilbert space of complex-valued functions

$$u_2(\mathbf{x}_1, t_1; \mathbf{x}_2, t_2) = \sum_{\mathbf{l}_{\mathbf{x}_1}} \sum_{l_{t_1}} \sum_{\mathbf{l}_{\mathbf{x}_2}} \sum_{l_{t_2}} d_{\mathbf{l}_{\mathbf{x}_1} l_{t_1} \mathbf{l}_{\mathbf{x}_2} l_{t_2}} e_{\mathbf{l}_{\mathbf{x}_1}}(\mathbf{x}_1) e_{l_{t_1}}(t_1) e_{\mathbf{l}_{\mathbf{x}_2}}(\mathbf{x}_2) e_{l_{t_2}}(t_2) \quad (74)$$

over the domain \mathbb{D}^2 .

Note that $\dim(\mathcal{H}_2^p) = (\dim(\mathcal{H}_1^p))^2$.

C Encoding of Spatiotemporal Stimuli with a Population of Complex Cells

We consider again a neural circuit consisting of a population of M neurons modeling a population of complex cells as illustrated in Figure 1. The input to the neural circuit is spatiotemporal stimulus as defined in Section B.

The input stimulus $u_1(\mathbf{x}, t)$ to neuron i is first processed by two spatio-temporal linear filters whose impulse responses are denoted, by abuse of notation, as $g_1^{i1}(\mathbf{x}, t)$ and $g_1^{i2}(\mathbf{x}, t)$, respectively. The output of the linear filters are squared and summed. The sum $v^i(t)$, as the output of the DSP, is then fed into the BSG of neuron i . The BSG encodes the DSP output into the spike train $(t_k^i)_{k \in \mathbb{I}^i}$. Here \mathbb{I}^i is the spike train index set of neuron i .

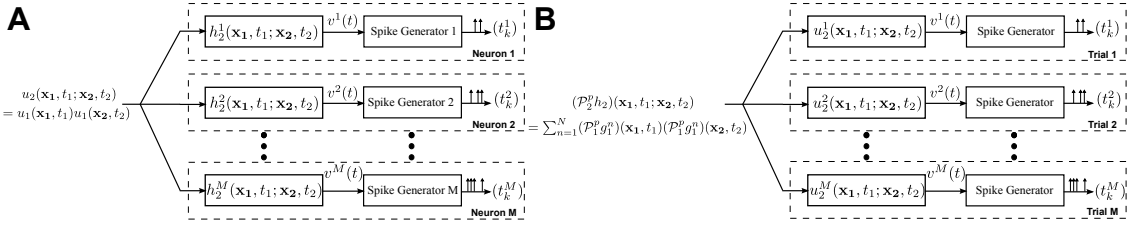


Figure 17: Duality between low-rank decoding and low-rank functional identification for spatio-temporal complex cells. (A) decoding of spatio-temporal stimuli encoded by a neural circuit of M complex cells and (B) functional identification of spatio-temporal complex cells by presenting M trials of stimuli.

Similar to the temporal case, the neural circuit is equivalent to that shown in Figure 17A. Here, the output of the DSP for each neuron $i = 1, 2, \dots, M$, can be expressed as

$$v^i(t) = \int_{\mathbb{D}^2} h_2^i(\mathbf{x}_1, t - s_1; \mathbf{x}_2, t - s_2) u_1(\mathbf{x}_1, s_1) u_1(\mathbf{x}_2, s_2) d\mathbf{x}_1 d\mathbf{x}_2 ds_1 ds_2. \quad (75)$$

Here

$$h_2^i(\mathbf{x}_1, t_1; \mathbf{x}_2, t_2) = g_1^{i1}(\mathbf{x}_1, t_1)g_1^{i1}(\mathbf{x}_2, t_2) + g_1^{i2}(\mathbf{x}_1, t_1)g_1^{i2}(\mathbf{x}_2, t_2) \quad (76)$$

is the low-rank DSP [18]. The encoding of stimulus by the neural circuit with complex cells is a special case of the low-rank DSP of the form given in (76). When using IAF point neurons as models of the BSGs, we have the following theorem describing the encoding of stimuli.

Lemma 3. *The encoding of stimulus $u_1 \in \mathcal{H}_1^p$ into the spike train sequence $(t_k^i), k \in \mathbb{I}^i, i = 1, 2, \dots, M$, by a neural circuit of spatio-temporal complex cells is given in functional form by*

$$\mathcal{T}_k^i u_2 = q_k^i, k \in \mathbb{I}^i, i = 1, \dots, M, \quad (77)$$

where $\mathcal{T}_k^i : \mathcal{H}_2^p \rightarrow \mathbb{R}$, are bounded linear functionals defined by

$$\mathcal{T}_k^i u_2 = \int_{t_k^i}^{t_{k+1}^i} \int_{\mathbb{D}^2} h_2^i(\mathbf{x}_1, t - s_1; \mathbf{x}_2, t - s_2) u_2(\mathbf{x}_1, s_1; \mathbf{x}_2, s_2) d\mathbf{x}_1 d\mathbf{x}_2 ds_1 ds_2 dt, \quad (78)$$

with $u_2(\mathbf{x}_1, t_1; \mathbf{x}_2, t_2) = u_1(\mathbf{x}_1, t_1)u_1(\mathbf{x}_2, t_2)$. Finally, $q_k^i = \kappa^i \delta^i - b^i(t_{k+1}^i - t_k^i)$.

Proof: As in Lemma 1, the t-transform of the i -th IAF neuron is given by (6).

The relationship (77) follows after replacing $v^i(t)$ given in (75) in equation (6). \square

Similar to Remark 2, equation (77) shows that the encoding of a stimuli by the neural circuit with low-rank DSPs can be viewed as generalized sampling.

By abuse of notation, we denote by \mathbf{c} the vector representing the coefficients of u_1 in (73), and \mathbf{D} as the matrix representing the coefficients of u_2 in (74). We skip here the detailed entries of \mathbf{c} and \mathbf{D} due to the complexity of the indices, but their construction follows closely with (28) and (26), respectively, and $\mathbf{D} = \mathbf{cc}^H$.

Theorem 5. Encoding the stimulus $u_1 \in \mathcal{H}_1^p$ with the neural circuit with complex cells given in (75) into the spike train sequence $(t_k^i), k \in \mathbb{I}^i, i = 1, 2, \dots, M$, satisfies the set of equations

$$\text{Tr}(\Phi_k^i \mathbf{D}) = q_k^i, k \in \mathbb{I}^i, i = 1, \dots, M, \quad (79)$$

where $\mathbf{D} = \mathbf{c}\mathbf{c}^H$ is a rank-1 Hermitian matrix and $(\Phi_k^i), k \in \mathbb{I}^i, i = 1, \dots, M$, are Hermitian matrices. $[\Phi_k^i]_{\mathbf{l}_{\mathbf{x}_2} l_{t_2}; \mathbf{l}_{\mathbf{x}_1} l_{t_1}}$ denotes the entry at the

$((l_{t_2} + L_{t_2} + 1) \prod_{i=1}^p (L_{x_{i2}} + 1) + \sum_{j=1}^p (l_{x_{j2}} + L_{x_{j2}} + 1) \prod_{i=1}^{j-1} (2L_{x_{i2}} + 1))$ -th row and the
 $((l_{t_1} + L_{t_1} + 1) \prod_{i=1}^p (L_{x_{i1}} + 1) + \sum_{j=1}^p (l_{x_{j1}} + L_{x_{j1}} + 1) \prod_{i=1}^{j-1} (2L_{x_{i1}} + 1))$ -th column, and

$$[\Phi_k^i]_{\mathbf{l}_{\mathbf{x}_2} l_{t_2}; \mathbf{l}_{\mathbf{x}_1} l_{t_1}} = \int_{t_k^i}^{t_{k+1}^i} e_{l_{t_1} - l_{t_2}}(t) dt \int_{\mathbb{D}^2} h_2^i(\mathbf{x}_1, s_1; \mathbf{x}_2, s_2) e_{\mathbf{l}_{\mathbf{x}_1}, -l_{t_1}}(\mathbf{x}_1, s_1) e_{-\mathbf{l}_{\mathbf{x}_2}, l_{t_2}}(\mathbf{x}_2, s_2) d\mathbf{x}_1 ds_1 d\mathbf{x}_2 ds_2, \quad (80)$$

where $\mathbf{l}_{\mathbf{x}_i} = (l_{x_{1i}}, l_{x_{2i}}, \dots, l_{x_{pi}}), i = 1, 2$.

Proof: Plugging in the general form of u_2 in (74) into (78), the left hand side of (77) amounts to

$$\begin{aligned} & \sum_{\mathbf{l}_{\mathbf{x}_1}} \sum_{l_{t_1}} \sum_{\mathbf{l}_{\mathbf{x}_2}} \sum_{l_{t_2}} d_{\mathbf{l}_{\mathbf{x}_1}, l_{t_1}, -\mathbf{l}_{\mathbf{x}_2}, -l_{t_2}} \int_{t_k^i}^{t_{k+1}^i} e_{l_{t_1} - l_{t_2}}(t) dt \cdot \\ & \quad \cdot \int_{\mathbb{D}^2} h_2^i(\mathbf{x}_1, s_1; \mathbf{x}_2, s_2) e_{\mathbf{l}_{\mathbf{x}_1}, -l_{t_1}}(\mathbf{x}_1, s_1) e_{-\mathbf{l}_{\mathbf{x}_2}, l_{t_2}}(\mathbf{x}_2, s_2) d\mathbf{x}_1 d\mathbf{x}_2 ds_1 ds_2. \end{aligned}$$

It is easy to verify that the expression above can be written as

$$\sum_{\mathbf{l}_{\mathbf{x}_1}} \sum_{l_{t_1}} \sum_{\mathbf{l}_{\mathbf{x}_2}} \sum_{l_{t_2}} d_{\mathbf{l}_{\mathbf{x}_1}, l_{t_1}, -\mathbf{l}_{\mathbf{x}_2}, -l_{t_2}} [\Phi_k^i]_{\mathbf{l}_{\mathbf{x}_2} l_{t_2}; \mathbf{l}_{\mathbf{x}_1} l_{t_1}} = \text{Tr}(\Phi_k^i \mathbf{D}), \quad (81)$$

where the

$((l_{t_1} + L_{t_1} + 1) \prod_{i=1}^p (L_{x_{i1}} + 1) + \sum_{j=1}^p (l_{x_{j1}} + L_{x_{j1}} + 1) \prod_{i=1}^{j-1} (2L_{x_{i1}} + 1))$ -th row
 $((l_{t_2} + L_{t_2} + 1) \prod_{i=1}^p (L_{x_{i2}} + 1) + \sum_{j=1}^p (l_{x_{j2}} + L_{x_{j2}} + 1) \prod_{i=1}^{j-1} (2L_{x_{i2}} + 1))$ -th column entry of
 \mathbf{D} amounts to $[\mathbf{D}]_{\mathbf{l}_{\mathbf{x}_1} l_{t_1}; \mathbf{l}_{\mathbf{x}_2} l_{t_2}} = d_{\mathbf{l}_{\mathbf{x}_1}, l_{t_1}, -\mathbf{l}_{\mathbf{x}_2}, -l_{t_2}}$.

Since $u_2(\mathbf{x}_1, t_1; \mathbf{x}_2, t_2) = u_1(\mathbf{x}_1, t_1)u_1(\mathbf{x}_2, t_2)$ and $d_{\mathbf{l}_{\mathbf{x}_1}, l_{t_1}, -\mathbf{l}_{\mathbf{x}_2}, -l_{t_2}} = c_{\mathbf{l}_{\mathbf{x}_1}, l_{t_1}} c_{\mathbf{l}_{\mathbf{x}_2}, l_{t_2}}^H$, thereby $\mathbf{D} = \mathbf{c}\mathbf{c}^H$. We also note that since $h_2^i, i = 1, \dots, M$, are assumed to be real valued, $(\Phi_k^i), k \in \mathbb{I}^i, i = 1, \dots, M$, are Hermitian. \square

Low-Rank Decoding of Spatio-Temporal Visual Stimuli

When using an algorithm similar to Algorithm 1 to reconstruct spatio-temporal stimuli encoded by a neural circuit with complex cells, at least $\dim(\mathcal{H}_1^p)(\dim(\mathcal{H}_1^p) + 1)/2$ measurements are required. In addition, at least $\dim(\mathcal{H}_1^p)(\dim(\mathcal{H}_1^p) + 1)/(4L_t + 1)$ neurons are

required, a number that can become unrealistically high with an increasing dimension of the input space.

With the observation that $\mathbf{D} = \mathbf{c}\mathbf{c}^H$ is a rank-one matrix, we can apply algorithms similar to those described in Section 3.1.2 to recover spatio-temporal stimuli encoded by a population of spiking neurons with low-rank DSPs.

D Low-Rank Functional Identification of Spatio-Temporal Complex Cells

Similar to Section 3.2, we consider here the identification of low-rank DSP of complex cells from spike times generated when multiple stimulus trials are presented. We first define the projection operators in \mathcal{H}_1^p . Then, based on (75), we show that the duality between decoding and functional identification also holds in the spatio-temporal case.

Definition 6. Let $h_n \in \mathbb{L}^1(\mathbb{D}^n)$, $n = 1, 2$, where \mathbb{L}^1 denotes the space of Lebesgue integrable functions. The operator $\mathcal{P}_1^p : \mathbb{L}_1(\mathbb{D}) \rightarrow \mathcal{H}_1^p$ given by

$$(\mathcal{P}_1^p h_1)(\mathbf{x}, t) = \int_{\mathbb{D}} h_1(\mathbf{x}', t') K_1^p(\mathbf{x}, t; \mathbf{x}', t') d\mathbf{x}' dt' \quad (82)$$

is called the projection operator from $\mathbb{L}^1(\mathbb{D})$ to \mathcal{H}_1^p . Similarly, the operator $\mathcal{P}_2^p : \mathbb{L}_1(\mathbb{D}^2) \rightarrow \mathcal{H}_2$ given by

$$(\mathcal{P}_2^p h_2)(\mathbf{x}_1, t_1; \mathbf{x}_2, t_2) = \int_{\mathbb{D}^2} h_2(\mathbf{x}_1', t_1'; \mathbf{x}_2', t_2') K_2^p(\mathbf{x}_1, t_1; \mathbf{x}_2, t_2; \mathbf{x}_1', t_1'; \mathbf{x}_2', t_2') d\mathbf{x}_1' d\mathbf{x}_2' dt_1' dt_2' \quad (83)$$

is called the projection operator from $\mathbb{L}^1(\mathbb{D}^2)$ to \mathcal{H}_2 .

We consider here complex cells whose low-rank DSP can be expressed more generally as

$$h_2(\mathbf{x}_1, t_1; \mathbf{x}_2, t_2) = \sum_{n=1}^N g_1^n(\mathbf{x}_1, t_1) g_1^n(\mathbf{x}_2, t_2), \quad (84)$$

where, by abuse of notation, $g_1^n(\mathbf{x}, t)$, $n = 1, \dots, N$ are impulse responses of spatio-temporal linear filters, and $N \ll \dim(\mathcal{H}_1^p)$. Similar to the approach we take in Section 3.2, this particular structure can be exploited to identify the projection of h_2 using tractable algorithms.

By abuse of notation, we denote \mathbf{g}^n as the vector representing the coefficients of $\mathcal{P}_1^p g_1^n$, and \mathbf{H} as the matrix representing the coefficients of $\mathcal{P}_2^p h_2$. The detailed entries of \mathbf{g}^n and \mathbf{H} are constructed similarly to (48) and (49), respectively. In addition, we have $\mathbf{H} = \sum_{n=1}^N \mathbf{g}^n (\mathbf{g}^n)^H$.

Theorem 6. By presenting M trials with stimuli $u_2^i(\mathbf{x}_1, t_1; \mathbf{x}_2, t_2) = u_1^i(\mathbf{x}_1, t_1) u_1^i(\mathbf{x}_2, t_2)$, $i = 1, \dots, M$, to a complex cell and observing the spike trains t_k^i , $k \in \mathbb{I}^i$, $i = 1, 2, \dots, M$, the coefficients of the projections $\mathcal{P}_2^p h_2$ of the DSP of the complex cell, satisfy the set of equations

$$\text{Tr}(\Psi_k^i \mathbf{H}) = q_k^i, \quad k \in \mathbb{I}^i, \quad i = 1, \dots, M, \quad (85)$$

where \mathbf{H} is a rank- N positive semidefinite Hermitian matrix and (Ψ_k^i) , $k \in \mathbb{I}^i$, $i = 1, \dots, M$, are Hermitian matrices with the entry at the

$\left((l_{t_2} + L_{t_2} + 1) \prod_{i=1}^p (L_{x_{i2}} + 1) + \sum_{j=1}^p (l_{x_{j2}} + L_{x_{j2}} + 1) \prod_{i=1}^{j-1} (2L_{x_{i2}} + 1) \right)$ -th row and the
 $\left((l_{t_1} + L_{t_1} + 1) \prod_{i=1}^p (L_{x_{i1}} + 1) + \sum_{j=1}^p (l_{x_{j1}} + L_{x_{j1}} + 1) \prod_{i=1}^{j-1} (2L_{x_{i1}} + 1) \right)$ -th column given by
 $[\Psi_k^i]_{\mathbf{l}_{\mathbf{x}_2} l_{t_2}; \mathbf{l}_{\mathbf{x}_1} l_{t_1}} =$

$$\int_{t_k^i}^{t_{k+1}^i} e_{l_{t_1}, -l_{t_2}}(t) dt \int_{\mathbb{D}^2} u_2^i(\mathbf{x}_1, s_1; \mathbf{x}_2, s_2) e_{\mathbf{l}_{\mathbf{x}_1}, -l_{t_1}}(\mathbf{x}_1, s_1) e_{-\mathbf{l}_{\mathbf{x}_2}, l_{t_2}}(\mathbf{x}_2, s_2) d\mathbf{x}_1 ds_1 d\mathbf{x}_2 ds_2, \quad (86)$$

where $\mathbf{l}_{\mathbf{x}_i} = (l_{x_{1i}}, l_{x_{2i}}, \dots, l_{x_{pi}})$, $i = 1, 2$.

Proof: Essentially similar to the proof of Theorem 4.

Remark 13. Theorem 5 and Theorem 6 suggest that decoding of spatio-temporal stimuli encoded by a population of complex cells is dual to the functional identification of the DSP of complex cells presented with multiple stimulus trials. This is further illustrated in Figure 17. Note that in identification, only the projection of the complex cell DSP onto the stimulus space can be identified.

Based on Theorem 6, we can formulate functional identification algorithms for complex cell DSPs of the form (84) with a significant reduction in the number of required trials and spikes. The algorithms are similar to those presented in Section 3.2.2.